Review paper

First-Principles Exploration of Magnetic, Thermal and Hydrogen Storage Properties in Alkali-Based $XHfH_3$ Perovskites

Nasir Ali[1], Shah Zeb Ullah[1, 2, *], Muneeb Ur Rehman[1], Danish Rehman[1], Ahmad Junaid[1], Muhammad Yasir Akhtar[1], Mujtaba Ali[1]

[1] Department of Physics, Government Postgraduate College Kohat, KP, Pakistan
[2] Department of Physics, Kohat University of Science and Technology Kohat, KP, Pakistan

***** *Corresponding author:* ph420222002@kust.edu.pk, shahzebkhan2917@gmail.com

Abstract: The development of effective hydrogen storage materials is vital for the implementation of sustainable and carbon-neutral energy solutions. Solid-state hydrides have emerged as an attractive option because of their enhanced safety and volumetric efficiency compared to traditional compressed and liquefied hydrogen systems. Modest storage performance and elevated desorption temperatures remain key barriers to practical implementation. In this study, a comprehensive first-principles analysis based on density functional theory (DFT) was conducted to evaluate the structural, electronic, phonon, magnetic, thermal, and hydrogen storage properties of $XHfH_3$ (X = Li, Na, and Rb) perovskite hydrides. Structural optimization confirmed thermodynamic stability, with lattice parameters exhibiting a gradual increase from Li to Rb, consistent with the corresponding increase in ionic radii. Electronic band structure and density of states investigations reveal a metallic nature for all compounds. Following structural relaxation, $NaHfH_3$ and $RbHfH_3$ retain magnetic moments with integral spin densities of approximately 2.05 μB and 2.08 μB, respectively. Mechanical stability is confirmed by computed elastic constants satisfying the Born stability criterion. Phonon dispersion simulations demonstrate dynamic stability exclusively for $RbHfH_3$, whereas $LiHfH_3$ and $NaHfH_3$ exhibit imaginary frequencies indicative of lattice instabilities. The high-frequency vibrational modes are largely associated with hydrogen atoms, significantly influencing lattice dynamics and thermodynamic behavior. Furthermore, molecular dynamics simulations confirm the thermal stability of the materials. Collectively, the $XHfH_3$ family exhibits tunable magnetic, vibrational, thermal, and hydrogen-storage-related behavior, making these compounds useful model systems for understanding alkali-site effects in hafnium-based hydride perovskites, although their high predicted desorption temperatures limit immediate practical hydrogen-storage applicability.

Keywords: Anisotropy; Debye temperature; Magnetic properties; Mechanical properties; Metal hydride

1. Introduction

Energy storage is an essential part of modern energy systems since the world progressively switches from fossil fuels to renewable energy sources [1]. Regular energy needs can be met using energy produced from renewable resources. In order to comply with international conventions on carbon dioxide emissions, the use of fossil fuels is decreasing while the use of renewable energy is increasing rapidly [2]. Hydrogen is a promising alternative to fossil fuels, but its storage remains a challenge. Compressed hydrogen shows potential for mobile applications but faces challenges in volumetric density, safety, and cost. Cryo-compressed storage synergistically addresses refueling speed, boil-off, and energy efficiency, making it suitable for onboard use. Material-based methods offer improved energy density, safety, and weight savings, though stability and capacity require further development [3, 4].

The rising adoption of perovskite hydride materials for hydrogen storage stems from the critical demand for robust storage technologies that can accommodate intermittent renewable energy sources, thereby playing a key role in advancing sustainable energy systems [5]. Perovskite-type structures offer considerable potential to develop solar cell applications and hydrogen storage technology, providing a strong base for further advancements in these key domains [6-8].

DOI: https://doi.org/10.66173/jenmas.2026.79
Received 17 March 2026, Revised 27 April 2026, Accepted 28 April 2026, Available online 7 May 2026

It is noted that perovskite hydrides store absorbed hydrogen within their intricate crystal lattice, enabling stable and high-capacity hydrogen storage. Dehydrogenation is induced upon the application of heat or reduction in pressure [9]. Recent efforts to improve the hydrogen storage properties of perovskite hydrides have focused on strategies such as elemental substitution (doping) and the construction of composite material systems. The developmental history of these materials spans from early experimental synthesis and characterization to contemporary theoretical predictions and performance optimization approaches, including high-throughput computational screening and machine-learning-assisted design [10].

The inadequacy of conventional intermetallic alloys in meeting required hydrogen storage capacities [11] has prompted increased interest in perovskite-type hydrides, particularly given that renewable and eco-friendly hydrogen energy is a critical need for automotive applications [12]. Among the reported perovskite hydrides, platinum-based compounds ($LiPtH_3$, $NaPtH_3$, $KPtH_3$, and $RbPtH_3$) exhibit gravimetric capacities ranging from 1.06 to 1.45 wt.% [13]. Higher values are observed for zirconium-based perovskites, with $CaZrH_3$ achieving 2.251 wt.%, followed by $SrZrH_3$ at 1.662 wt.% and $BaZrH_3$ at 1.307 wt.% [14]. According to the literature, perovskite hydrides exhibit a wide range of hydrogen storage capacities depending on their elemental composition. For instance, $CaRhH_3$ and $BaRhH_3$ not only show strong optical responses but also deliver 2.07 wt.% and 1.24 wt.% hydrogen storage, respectively [15]. Among Rb-based 5d transition metal hydrides, Ta, W, and Re offer comparable densities around 1.13-1.12 wt.% [16]. Despite not achieving DOE targets (1.46-2.59 wt.% range), these materials are valued for their stability, kinetic performance, and mechanical robustness, positioning them as viable candidates for niche, small-to-medium capacity applications [17]. The Cs-based family ($CsCaH_3$, $CsSrH_3$, $CsBaH_3$) further contributes capacities of 1.71, 1.33, and 1.11 wt.%, respectively [18]. The development of perovskite-structured metal borohydrides enables precise regulation of metal ion electronegativity within a single framework, effectively lowering the dehydrogenation temperature [19]. Experimental results indicate that decorating ZrCo alloys with Hf improves their hydrogen storage performance [20]. Hafnium-based intermetallic compounds have been identified as highly promising candidates for reversible hydrogen storage applications [21].

Recently, Hammad et al. [22] reported a first-principles investigation of hafnium-based $XHfH_3$ perovskite hydrides, where X = Li, Na, K, and Rb, focusing mainly on their structural, electronic, mechanical, optical, and hydrogen-storage characteristics. Their study provides an important reference point for this compound family; however, the magnetic response, phonon-related dynamic stability, and temperature-dependent thermodynamic behavior of these materials remain insufficiently explored. In the present work, we therefore extend the understanding of $XHfH_3$ hydrides by examining $LiHfH_3$, $NaHfH_3$, and $RbHfH_3$ through spin-polarized electronic-structure calculations, phonon dispersion analysis, molecular dynamics simulations, and temperature-dependent thermal-property evaluation. This approach enables assessment of whether alkali-site substitution influences magnetic ordering, lattice stability, vibrational behavior, and thermal robustness. By clarifying these aspects, the study provides complementary insights into the fundamental physical behavior of alkali hafnium hydride perovskites and helps identify their limitations and potential relevance as model systems for future solid-state hydrogen-storage materials.

2. Computational Method

The three-dimensional structures of hydride perovskites $XHfH_3$ (X = Li, Na, Rb) were optimized using the CASTEP package with the plane-wave, pseudopotential framework of DFT [23, 24]. The Kohn–Sham equations were solved under periodic boundary conditions using a plane-wave basis set guided by Bloch's theorem, and Vanderbilt-type ultrasoft pseudopotentials were applied for electron-ion interactions [25, 26]. Structural optimization was performed using the Broyden-Fletcher-Goldfarb-Shanno (BFGS) minimization algorithm, which efficiently handles unconstrained nonlinear optimization [26]. Pulay density mixing was used throughout the self-consistent field (SCF) cycles to enhance convergence, particularly for systems with slow-converging electronic structures [27, 28]. Brillouin-zone integrations were carried out using a Monkhorst–Pack k-point mesh of $6 \times 6 \times 6$. A plane-wave cutoff energy of 500 eV was adopted. Convergence thresholds included a total-energy tolerance of 2×10^{-5} eV/atom, maximum ionic forces of 0.05 eV/Å, maximum stress below 0.1 GPa, and maximum ionic displacement of 2×10^{-3} Å. Elastic constants and mechanical stability were evaluated using the PBE-GGA functional. Strain stress calculations were performed in four cycles with a maximum strain amplitude of 0.003. The energy tolerance for elastic calculations was 4×10^{-6} eV/atom, with force and displacement limits of 0.01 eV/Å and 4×10^{-4} Å, respectively. High-precision convergence criteria were applied to both geometry optimization and elastic-constant calculations. All material properties were analyzed after complete unit-cell optimization.

Optical properties were computed using the GGA-PBE functional with a 6 × 6 × 6 k-point mesh and a 20.0 eV energy range. For metals or materials with very small band gaps, PBE's band gap error is less problematic, and its optical response can be qualitatively accurate. A band tolerance of 1.0×10^{-5} was applied. Calculations used x-polarized light (1.0, 0, 0), a 0.5 eV smearing, and no scissors correction. The plasma frequencies were tuned to 0 eV, and a Drude damping of 0.05 eV compensated for intraband contributions, guaranteeing correct optical spectra.

Phonon dispersion calculations were performed to evaluate the dynamic stability of the optimized $XHfH_3$ structures. The absence of imaginary phonon modes was taken as evidence of dynamic stability, whereas the presence of imaginary frequencies indicated lattice instability. The phonon spectra were analyzed along the high-symmetry path of the Brillouin zone for the cubic perovskite structure. In addition, molecular dynamics simulations were carried out using the FORCITE module in Materials Studio to examine finite-temperature structural stability. These simulations were classical molecular dynamics calculations based on the Universal Force Field, not ab initio molecular dynamics. The simulations were performed in the NVE ensemble at 298 K using random initial velocities, a 1.0 fs time step, and a total simulation time of 15 ps. Ewald summation was used for electrostatic interactions with an accuracy of 1.0×10^{-4} kcal mol^{-1} and a buffer width of 0.5 Å. The temperature and total-energy evolution were monitored to assess thermal equilibration and structural stability during the simulation.

3. Results and Discussion

3.1 Structural Properties

A material structural property is critical in defining its atomic-level stability and configurations. These properties are particularly crucial since they serve as the foundation for calculating equilibrium lattice parameters, which have an influence on a range of physical qualities. The material utilized in this work possesses cubic crystal symmetry, which fosters constant ionic covalent connections between X^{1+}, Hf^{2+} [29], and H^{1-} ions and adds to the overall lattice stabilization. The electronic structure of the component atoms are as follows: hydrogen (H) has a $1s^1$ configurations, the heavier anion Hafnium (Hf) has a [Xe] $4f^{14}$ $5d^2$ $6s^2$, configuration, and the X anions are the electron configuration: [He] $2s^1$ for lithium (Li), [Ne] $3s^1$ for sodium (Na), and [Kr] $5s^1$ for rubidium (Rb). As shown in Figure 1, the crystal structure and XRD pattern of the above-mentioned compound have a flexible framework and a 3D model.

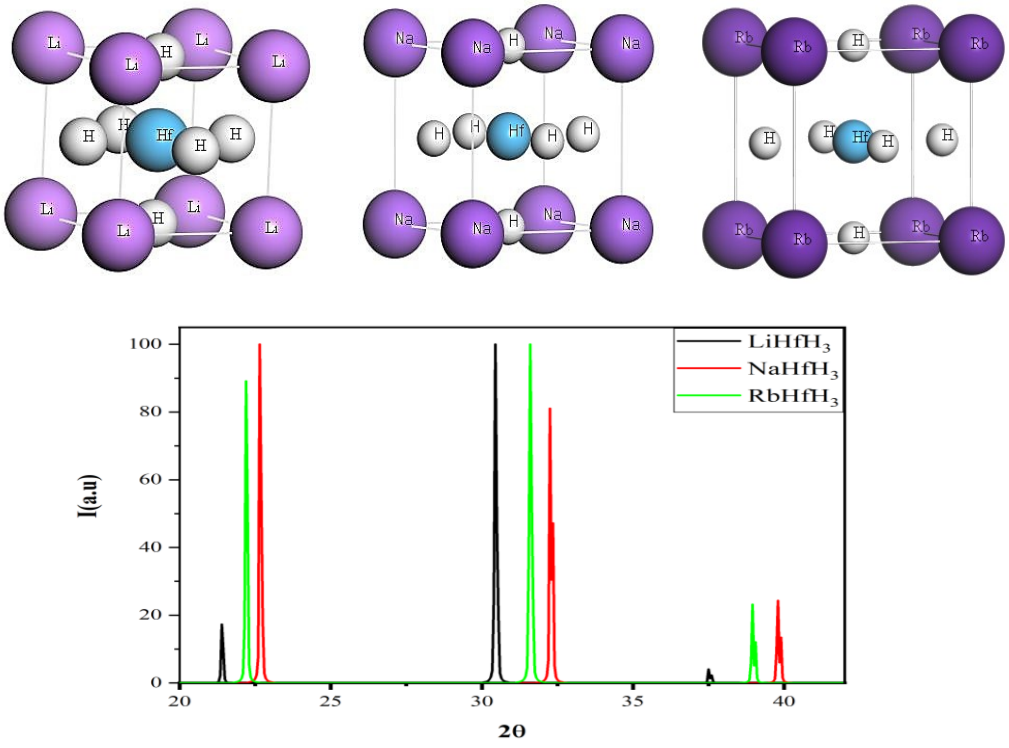

Figure 1. Optimized crystal structures and simulated X-ray diffraction patterns of $XHfH_3$ (X = Li, Na, Rb)

The total energy of the structure was calculated and used to determine important ground-state properties, including the crystal cell volume (lattice parameters) and the bulk modulus (B_0) at the equilibrium volume. To accurately fit **(S.1)** the calculated total energies, the Birch–Murnaghan equation of state [39] was applied, as expressed below:

$$E(V) = E(V_o) + \frac{B}{B'(B'-1)}\left[V\left(\frac{V_o}{V_P}\right)^{B'} - V_o\right] + \frac{B}{B'}(V - V_o) \quad (1a)$$

In equation 1a, E(V) represents the energy at a given volume V, while $E(V_0)$ denotes the total energy at the equilibrium volume V_o. The parameter B corresponds to the bulk modulus, and B′ represents the first derivative of the bulk modulus with respect to pressure.

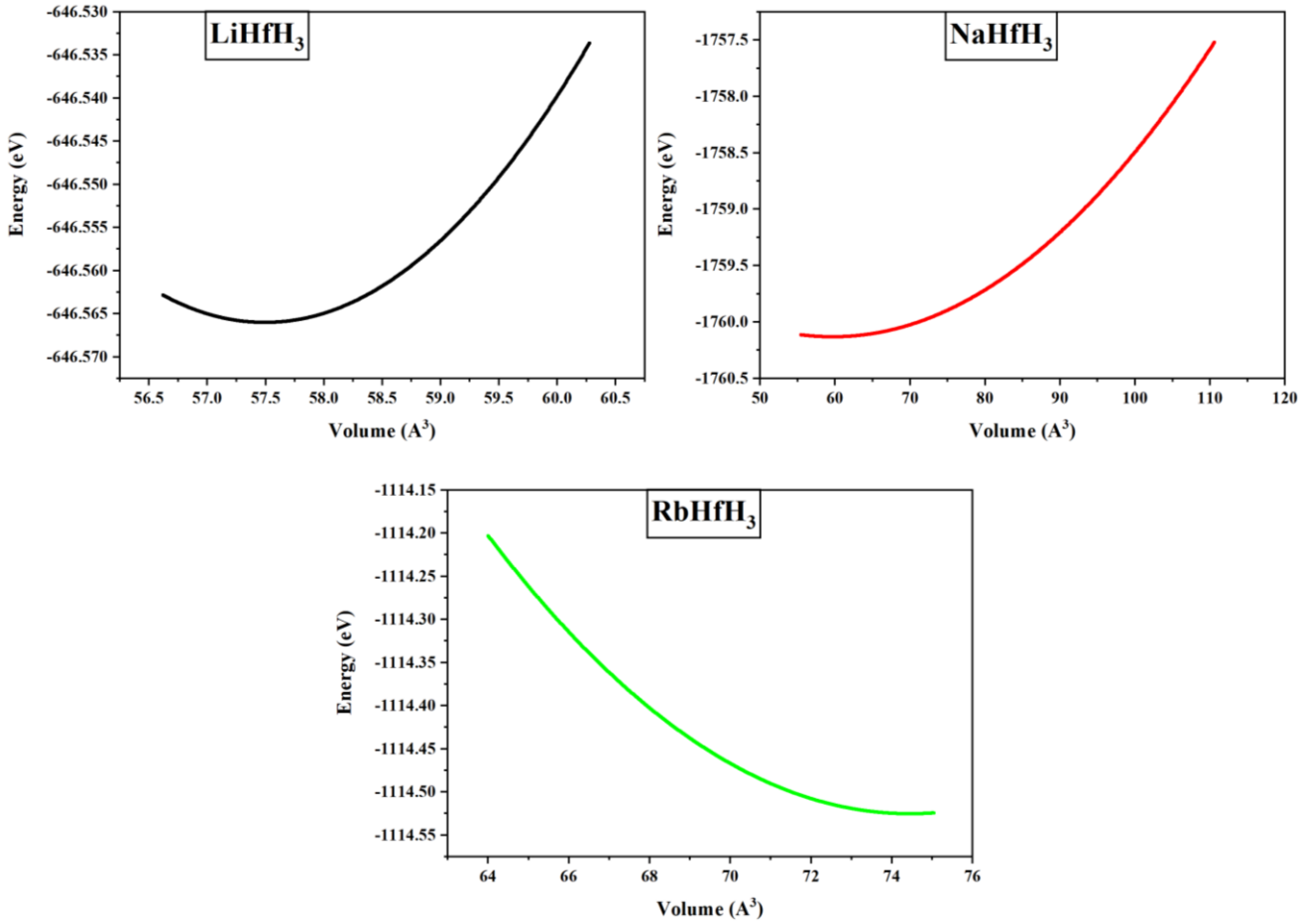

Figure S1. Murnaghan equation of state fitted to the calculated total energy as a function of volume

The Wyckoff position for X (Li, Na, Rb) is (0,0,0) and for Hf is (0.5, 0.5, 0.5) while for H is (0, 0.5,0.5). Each perovskite hydride unit cell was structurally optimized by adjusting its volume until the system attained the lowest total energy in order to determine the most energetically advantageous configurations. The optimized structural information is displayed in Table 1.

Table 1. The explored values of lattice constant, volume, and bandgap energy of $XHfH_3$

Samples	Lattice Constant (Å)	Volume (Å^3)	Density (amu/Å^3)	Formation energy (eV/atom)	Ref.
$LiHfH_3$	3.86	57.51	3.25	-3.95	This work
$NaHfH_3$	4.00	64.00	3.19	-3.71	This work
$RbHfH_3$	4.22	75.15	3.16	-3.46	This work
Y_2FeCrO_6	5.29	148.04	-	-3.12	[30]
$RbGaH_3$	4.08	67.69	-	-	[31]
$CsGaH_3$	4.21	74.82	-	-	[31]
$KMnH_3$	3.69	-	-	-8.11	[32]
$LiMnH_3$	3.29	-	-	-9.72	[32]
$BaMnH_3$	3.71	-	-	-23.24	[33]
$CaMnH_3$	2.36	-	-	-24.16	[33]

We calculated the formation energies of the investigated perovskite hydrides, which are the total energy difference between the compound and its isolated elemental components in their standard states, in order to assess their thermodynamic stability. A chemical is thermodynamically favorable and forms spontaneously if its formation energy is negative. $LiHfH_3$, $NaHfH_3$, and $RbHfH_3$ have calculated values of -3.9548, -3.7112, and -3.4619 eV/atom, respectively (see Table 1) [44]. These negative values imply that the formation processes of all three chemicals are exothermic and validate their thermodynamic stability.

$$\Delta E_f = \frac{E_{total}^{XHfH3} - \left[E_{total}^{X} + E_{total}^{Hf} + 3E_{total}^{H3}\right]}{N} \quad (1b)$$

In equation 1b, ΔE_f represents the formation energy, while the compound's total ground-state energy is denoted by E_{total}. The energy of the separated component atoms is indicated by the letters E^X, E^{Li}, and $E^H{}_2$. Since all three of the $XHfH_3$ (X = Li, Na, and Rb) compounds have negative estimated formation energies, it can be said that these hydrides are thermodynamically stable and that their creation processes are exothermic.

Figure 1 presents the simulated X-ray diffraction patterns of $LiHfH_3$, $NaHfH_3$, and $RbHfH_3$ in the 2θ range of 20–42° using Cu Kα radiation (λ = 1.5406 Å). These simulated patterns provide theoretical diffraction fingerprints for the optimized cubic structures and may serve as useful references for future experimental identification. The main diffraction peaks were indexed using Bragg's law, $n\lambda = 2d\sin\theta$, together with the cubic interplanar spacing relationship. Since the present study is computational, the simulated XRD patterns should be interpreted as structural signatures predicted from the optimized models rather than as experimental confirmation of phase purity [34].

Table 2. X-ray Diffraction data for $XHfH_3$ compound, including 2θ angle, Miller indices (hkl), and observed peak intensities

Compound	2θ (°)	Plane (hkl)	Intensity (a.u.)
$LiHfH_3$	30.4	(100)	High
	21.4	(110)	Medium
	37.5	(200)	Low
$NaHfH_3$	22.7	(100)	High
	32.3	(110)	Medium
	39.9	(200)	Low

The simulated XRD patterns show characteristic diffraction peaks for the optimized $LiHfH_3$, $NaHfH_3$, and $RbHfH_3$ structures. For $LiHfH_3$, the main reflections appear at $2\theta = 21.4°$, 30.4°, and 37.5°, while $NaHfH_3$ exhibits peaks at 22.7°, 32.3°, and 39.9°. For $RbHfH_3$, the predicted peaks appear at 22.2°, 31.6°, and 38.9°. The systematic shift in peak positions across the series is consistent with lattice expansion caused by the increasing ionic radius of the alkali-metal cation from Li to Rb. Variations in peak intensity may be attributed to differences in atomic scattering factors, particularly the stronger scattering contribution from heavier Rb atoms. Overall, the simulated XRD results support the structural consistency of the optimized cubic $XHfH_3$ models and provide reference patterns for future experimental validation [35]. [36].

Figure 2 presents the time evolution of temperature and total energy for $LiHfH_3$, $NaHfH_3$, and $RbHfH_3$ obtained from molecular dynamics simulations, providing insight into their thermal stability and equilibration behavior. The temperature profiles for all three compounds fluctuate around their target values with no systematic drift over the simulation time (15 ps), indicating that the systems have reached thermal equilibrium. However, the magnitude of fluctuations differs slightly among the materials. $LiHfH_3$ and $NaHfH_3$ exhibit comparatively larger temperature oscillations, suggesting relatively higher lattice sensitivity and possible anharmonic effects. In contrast, $RbHfH_3$ shows more uniform fluctuations, reflecting improved thermal stability and better energy distribution within the lattice.

The total energy plots added up keep these observations. All systems display well-converged energy profiles with small oscillations around a constant mean value, confirming the absence of energy drift and the reliability of the simulations. Notably, $RbHfH_3$ demonstrates relatively smoother energy fluctuations, indicating a more stable potential energy surface. Meanwhile, $LiHfH_3$ and $NaHfH_3$ show slightly larger deviations, which may be associated with their previously identified lattice instabilities from phonon analysis. $RbHfH_3$ is thus the most thermodynamically stable choice among the compounds investigated for use in hydrogen storage.

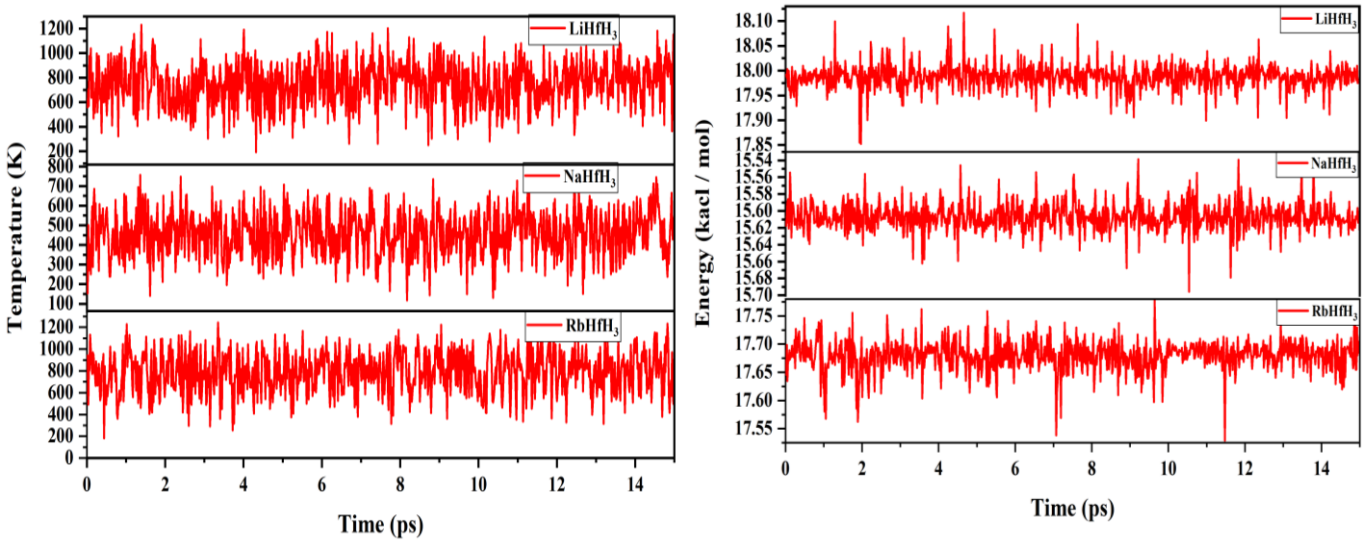

Figure 2. Time evolution of temperature and total energy of $XHfH_3$ (X = Li, Na, Rb)

3.2 Hydrogen Storage Capacity

The gravimetric hydrogen storage capacity Cwt.% of $XHfH_3$ (X = Li, Na, Rb) hydride-perovskite is determined using a theoretical equation, assessing its applicability for hydrogen storage devices. The mass of deposited hydrogen in proportion to the mass of the host perovskite is measured by the Cwt.% metric, which is determined by the following equation 2a [37, 38].

$$C_{wt.\%} = \left(\frac{\left(\frac{H}{M}\right) m_{Hydrogen}}{m_{Host} + \left(\frac{H}{M}\right) m_{Hydrogen}} \right) \quad (2a)$$

The equation practices the following symbols: H/M stands for the ratio of hydrogen atoms to composite atoms, $m_{Hydrogen}$ for the hydrogen molar mass, and m_{Host} for the host compounds molar-masses. The Cwt.% values, which are available in Table 3, show how much hydrogen the $XHfH_3$ (X = Li, Na, and Rb) perovskite can store. With a Cwt.% value of 1.61,1.48, and 1.13 for $XHfH_3$ (where X = Li, Na, and Rb), shows great promise as a viable option for applications involving the storage of hydrogen (H_2).

Table 3. Compounds with optimized parameters and compression using DFT

Compounds	E_g (eV)	$C_{wt.\%}$	Ref.	Method
$LiCaH_3$	2.37	4.40	[39]	DFT
$CsSnH_3$	Metal	1.18	[40]	DFT
$FrSnH_3$	Metal	0.87	[40]	DFT
$KPtH_3$	Metal	1.26	[13]	DFT
$RbPtH_3$	Metal	1.06	[13]	DFT
Sr_2H_3Cl	2.12	1.4	[41]	DFT
$BaRhH_3$	Metal	1.24	[15]	DFT
Ca_2FeH_5	Metal	1.5	[42]	DFT
$CsBaH_3$	2.24	1.10	[43]	DFT
$LiHfH_3$	Metal	1.61	This work	DFT
$NaHfH_3$	Metal	1.48	This work	DFT
$RbHfH_3$	Metal	1.13	This work	DFT

$LiHfH_3$, $NaHfH_3$, and $RbHfH_3$ demonstrate a 1.61 wt.%, 1.48 wt.%, and 1.13 wt.% hydrogen storage capacity, reaching 29, 26.9 %, and 20.5% of the U.S. DOE's 2025 interim objective (5.5 wt.%) and roughly 24 wt.% of the ultimate storage goal (6.5 wt.%) [44]. When it comes to operating circumstances and theoretically expected desorption temperatures, the material under study has notable benefits over traditional metal hydrides. The temperature at which hydrogen (H) must be released from a substance is known as the hydrogen desorption temperature. Equation 2b, which takes the hydrogen entropy change (ΔS) and formation enthalpy (ΔE_f) to be 130.7 J/mol·K, may be used to calculate this value [45]. By using this formula, the compound's desorption temperature is shown in Table 4.

$$T_{des} = \frac{\Delta E_f}{\Delta S} \tag{2b}$$

As the alkali-metal ionic size increases from Li to Rb, the gravimetric hydrogen-storage capacity of $XHfH_3$ decreases from 1.61 wt.% for $LiHfH_3$ to 1.48 wt.% for $NaHfH_3$ and 1.13 wt.% for $RbHfH_3$. A similar decreasing trend is observed in the predicted desorption temperature, with values of 1460 K, 1370 K, and 1278 K for $LiHfH_3$, $NaHfH_3$, and $RbHfH_3$, respectively. Although $RbHfH_3$ exhibits the lowest predicted desorption temperature among the three compounds, all calculated values remain very high for practical solid-state hydrogen-release applications. Therefore, these materials should be viewed primarily as model systems for understanding alkali-site effects on hydride stability, bonding, and lattice behavior, rather than as immediately practical hydrogen-storage materials. Future work should focus on strategies such as elemental substitution, defect engineering, nanostructuring, and catalytic modification to reduce the desorption temperature while retaining structural stability [46, 47].

Table 4. Predicted desorption temperatures of $XHfH_3$ compounds.

Materials	Desorption temperature T_{des} (K)	Ref.
$LiCrH_3$	3055.48 K	[45]
$KCrH_3$	2865.02 K	[45]
$CsCrH_3$	2610.34 K	[45]
$LiHfH_3$	1460 K	This work
$NaHfH_3$	1370 K	This work
$RbHfH_3$	1278 K	This work

The $XHfH_3$ perovskite is highly stable, with desorption temperature above 1278 K, comparable to their melting points, making solid-state hydrogen release impractical. Nevertheless, their structure robustness and stability trends offer insights into H-metal bonding and alkali-metal substitution, guiding future composition tuning for feasible hydrogen desorption [48, 49]. Additionally, hydrogen release behavior can be improved through several established strategies. Elemental substitution can tune thermodynamic stability and reduce desorption temperatures, while defect engineering enhances hydrogen diffusion pathways. Nano-structuring improves kinetics by shortening diffusion lengths, and catalyst incorporation lowers activation energy for hydrogen release. A synergistic combination of these approaches has been widely reported to enhance hydrogen storage performance [50-52].

3.3 Electronic Properties

The accessible energy levels where electrons can reside to regulate the electrical activity of compounds are determined by the band structure. Materials can be categorized as conductors, semiconductors, or insulators by looking at their band structure. Figure 3 shows the electrical band structure estimation for XHfH3. The Fermi level (FL) at the point of 0.0 eV is indicated by a blue horizontal line. The lower portion of FL is the valence band (V.B.) and the higher is the conduction band (C.B.), which are the two energy components that make up the materials framework. The compounds' band gap confirms their metallic character by showing that the valence and conduction bands overlap [53]. The metallic nature of all three compounds is confirmed by the lack of a noticeable separation between the occupied and unoccupied states. All of the constituent atoms contribute significantly to the conduction band of XHfH3, which spans from -25 eV to 0 eV. In the lower region is the valence band (-10 to -5 eV).

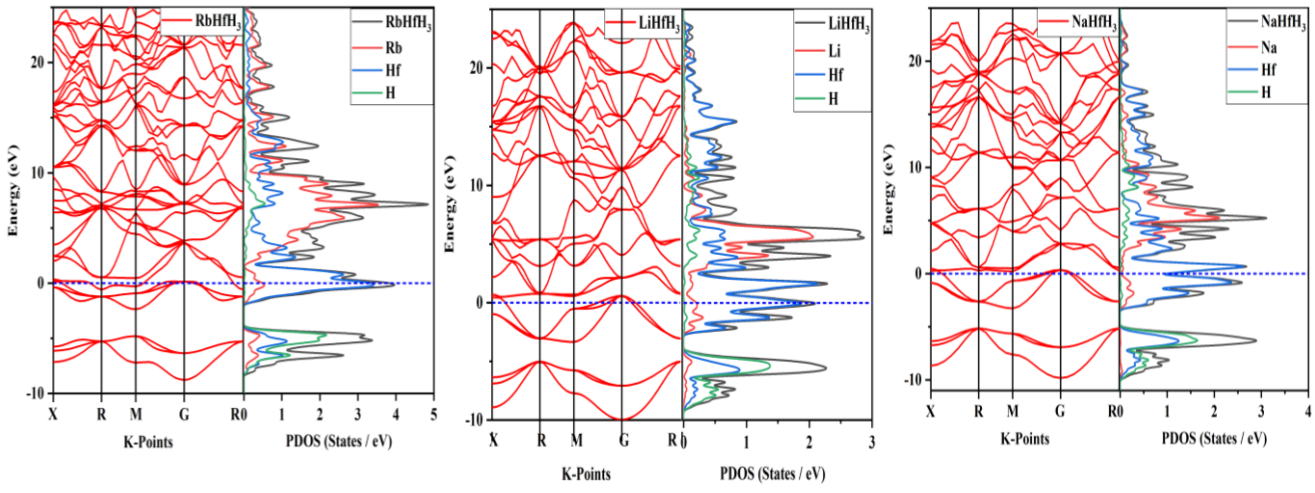

Figure 3. Electronic properties of $XHfH_3$(X=Li, Na, Rb) Band structure and PDOS.

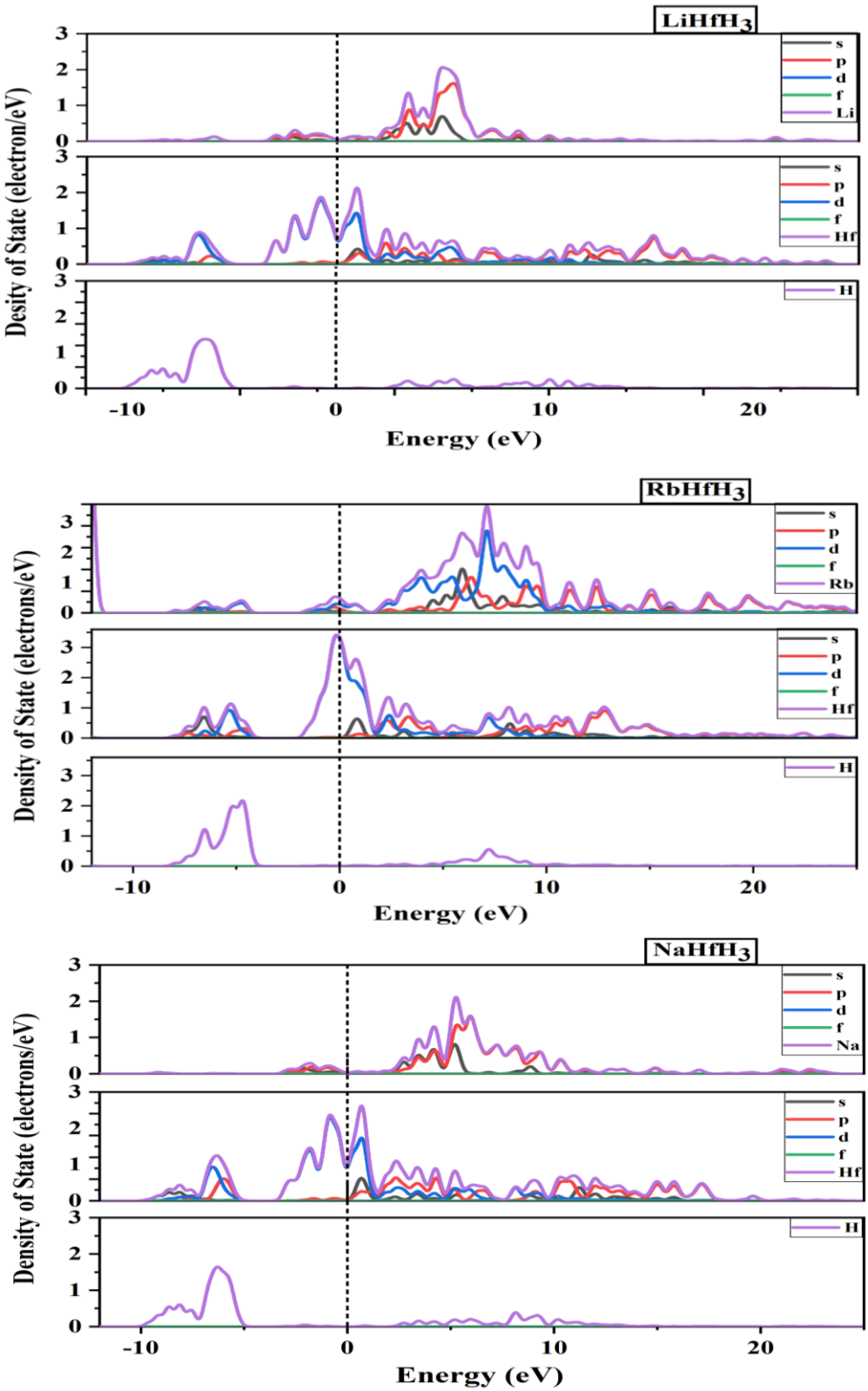

Figure 4. The partial density of state (PDOS) of $XHfH_3$ (where X = Li, Na, and Rb). The atomic orbital and total contribution of H (H-s), Hf and X (s, p, d, f)

Figure 4 depicts that the valence area is dominated by hafnium orbitals, suggesting that they play a crucial role in forming chemical bonds with both hydrogen and lithium atoms. Prominent peaks in the PDOS suggest the occurrence of Hf orbital-related localized bonding states. The orbitals of hafnium contribute considerably to the lower valence band but become increasingly important near the Fermi level, suggesting that they engage in bonding and potentially electronic conduction. Similarly, Li, Na, and Rb contribute more to the conduction band, which boosts the conductivity of the substance.

The PDOS study of $LiHfH_3$, $NaHfH_3$, and $RbHfH_3$ demonstrated a complicated yet systematic evolution of orbital interaction, where each orbital curve contributes differently to the electronic structure while preserving an overall metallic character across the series. In all three compounds, the deep valence region (-10 to -6 eV) is dominated by intense and well-defined H-1s peaks, showing strong and localized H-Hf and weak H-X bonding interaction that stabilize the lower-energy electronic states.

Table 5. Electronic structure investigation indicates a strong and concentrated XHfH3 bonding interaction.

Compound	H-H(Å)	Li-Li (Å)	X-Hf (Å)	H-Hf(Å)	H-X (Å)
$LiHfH_3$	2.773	3.921	3.396	1.96	2.773
$NaHfH_3$	2.830	4.330	3.466	2.001	2.830
$RbHfH_3$	2.982	4.217	3.652	2.109	2.982

Moving toward the upper valence bands (−6 to 0 eV), the PDOS becomes progressively hybridized, with significant Hf-d states overlapped with X-site s/p states. $LiHfH_3$ shows the highest hybridization, demonstrated by prominent Li-s and Li-p features around the Fermi level, which mix with Hf-d peaks to generate a denser electronic distribution. $NaHfH_3$ displays mild Na-p involvement, where the Na-derived curve occurs largely between −4 and 2 eV, indicating decreased but still present hybridization. In contrast, $RbHfH_3$ shows wide and weaker Rb-s/p states scattering throughout the valence and conduction band, corresponding with lower orbital overlaps due to the greater ionic radius of Rb.

Across all compounds, the Hf-d orbitals dominated the states near the Fermi level, creating the primary electronic component responsible for metallic conduction and defining both the valence-band maximum and the conduction-band minimums. The Hf-p and Hf-s curves give a small contribution dispersed throughout the valence bands, but X-d states remain insignificant in all situations. The conduction band (0 to 10 eV) is initiated by sharp Hf-d peaks just above the Fermi level, which are accompanied by weaker, more dispersed contributions from X-s/p orbital that become broader and less influential from Li → Na → Rb. This development, together with the observing diminishing intensity of H-s states and increasing localizations of X-p orbitals, implies a steady reduction in covalent X–H character and a matched rise in ionic nature over the series. Nevertheless, each combination preserves a limited DOS at the Fermi level dominated by Hf-d hybridized with residual H-s, and X-site states demonstrating strong metallicity across the $XHfH_3$ family.

The common behavior of all curves therefore suggests a clear trend where orbital hybridization strength, band propagation, and electronic quantity near the Fermi energy level are highest in $LiHfH_3$, intermediate in $NaHfH_3$, and weakest in $RbHfH_3$, reflecting an interplay in cation size, orbital overlap, and bonding character [54, 55].

The high-symmetry directions X–R–M–G–R in the Brillouin zone are used to determine the spin-polarized electronic band structures of $XHfH_3$ (X = Li, Na, and Rb), as seen in Figure. 5. At 0 eV, the Fermi level is fixed. The absence of an energy band gap and the metallic character of all three compounds are confirmed by the many electronic bands that cross the Fermi level in both spin channels. The intrinsic ferromagnetic ordering in these materials is shown by a distinct separation between the spin-up (↑) and spin-down (↓) bands close to the Fermi level, which results from exchange interactions [56, 57]. Throughout the Brillouin zone, especially in the vicinity of the G point, the spin degeneracy is removed, and at M points, where the spin-up and spin-down bands are more clearly separated. $LiHfH_3$ exhibits negligible spin polarization after structural relaxation, with a residual magnetic moment close to zero. Therefore, it is best described as essentially non-magnetic within the present spin-polarized DFT calculations [58]. In contrast, $NaHfH_3$ and $RbHfH_3$ retain finite magnetic moments of approximately 2.05 μB and 2.08 μB, respectively, suggesting the emergence of magnetic ordering as the alkali-metal ionic radius increases. It should be noted that

antiferromagnetic ordering was not explicitly examined in this work; therefore, the magnetic discussion is limited to the comparison between spin-polarized and nearly non-magnetic relaxed states.

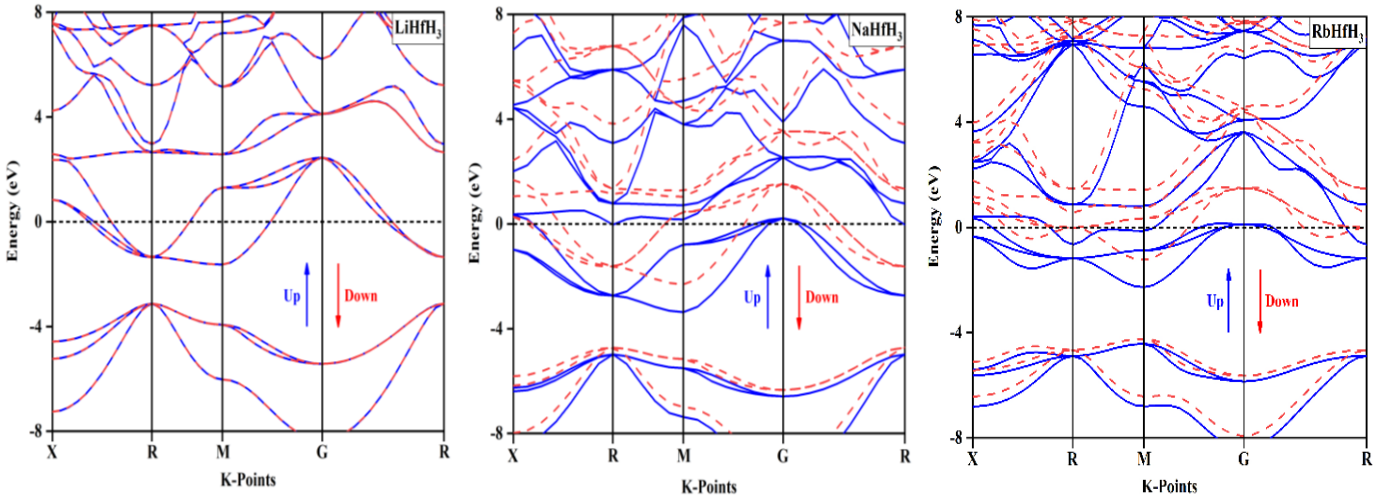

Figure 5. The spin-polarized band structures of $XHfH_3$.

The spin-polarized total density of states (DOS) of $XHfH_3$ (X = Li, Na, and Rb) compounds with the Fermi level set to zero energy. The presence of spin polarization and intrinsic magnetic behavior is shown in Figure 6 by the distinct asymmetry between the spin-up and spin-down DOS for each of the three systems. Interestingly, for at least one spin channel in each compound, a limited DOS occurs at the Fermi level, showing that $LiHfH_3$, $NaHfH_3$, and $RbHfH_3$ are metallic. Exchange splitting, characterized by a difference between spin-up and spin-down electronic states near the Fermi level, serves as an indicator of ferromagnetic ordering.

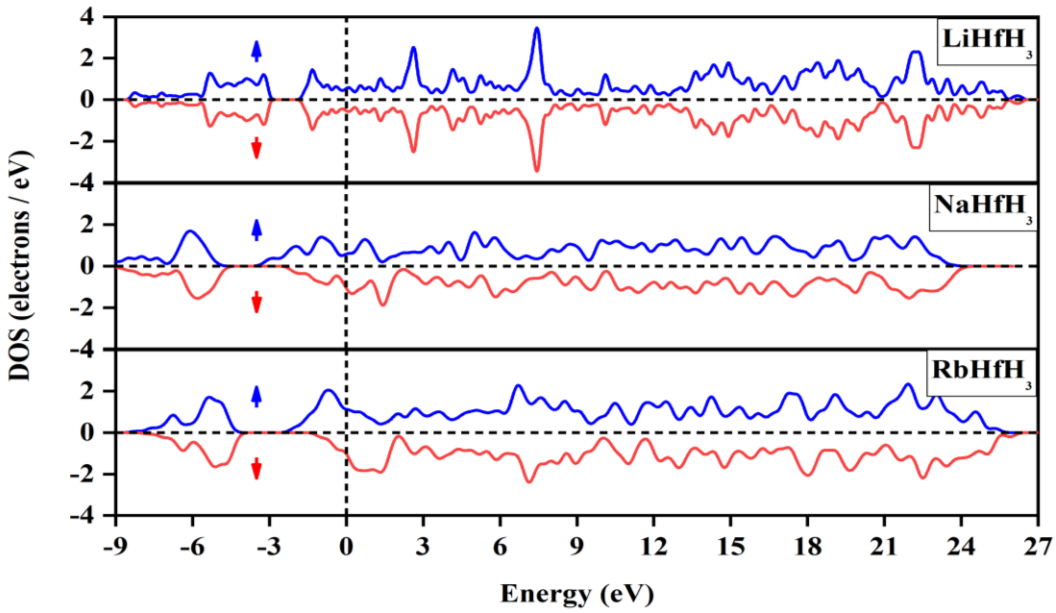

Figure 6. The spin-polarized density of states of $XHfH_3$.

Despite initializing all three compounds under spin-polarized conditions, only $NaHfH_3$ and $RbHfH_3$ sustain a net magnetic moment after complete structural relaxation, with computed total magnetic moments of approximately 2.05 μB and 2.08 μB, respectively. By contrast, $LiHfH_3$ is essentially non-magnetic, showing a residual spin density of merely ~10^{-6} μB. This behavior

correlates with the lattice expansion induced by increasing alkali-metal ionic size. Specifically, larger A-site cations diminish orbital overlap and strengthen the localization of Hf d electrons, thereby favoring the emergence of magnetic order in $NaHfH_3$ and $RbHfH_3$. Conversely, the smaller Li based molecules exhibit stronger hybridization and larger bands, which quench the magnetic moments. The results thus reveal a direct link between lattice parameter and magnetic stability in these perovskite hydrides [59].

3.4 Mechanical and Anisotropic Elastic Properties

The elastic constants (C_{ij}) of the material provide a complete description of its mechanical stability and, by extension, its industrial performance. CASTEP was used to calculate these constants. The crucial elastic constants for cubic structures are C_{11}, C_{44}, and C_{12}; these are listed in **Table 6** for $XHfH_3$ (Li, Na, Rb). The predicted values satisfy the stated Born stability criterion [60, 61], as in (4). The calculated results confirm that all stability conditions are satisfied. Specifically, the values of $C_{11} - C_{12}$ for $XHfH_3$ (Li, Na, Rb) are 132.42, 111.72, and 43.92 GPa, respectively, while the corresponding values of $C_{11}+2C_{12}$ are 162.99, 159.75, and 149.93 GPa. Moreover, all C_{11} and C_{44} values are positive, making them appropriate for further mechanical property calculations.

$$C_{11} > 0;\ C_{44} > 0;\ C_{11} - C_{12} > 0; \qquad C_{11} + 2C_{12} > 0 \tag{3}$$

Numerous physical properties, including as Young's modulus, shear modulus, and bulk modulus, may be obtained using the calculated elastic constants and are available in Table 6. The Voigt method was used to determine these moduli [62], Reuss [63], and Hill [64] approximations. The Hill approximation is the arithmetic mean of the modulus's greatest value, the lowest value is obtained by the Reuss technique, and the highest value is obtained by the Voigt method.

$$\mathrm{G} = \frac{1}{2}(\mathrm{G_V} + \mathrm{G_R}) \tag{4a}$$

$$G_V = \frac{1}{5}(C_{11} - C_{12} + 3C_{44}) \tag{4b}$$

$$G_R = \frac{5C_{44}(C_{11} - C_{12})}{4C_{44} + 3(C_{11} - C_{12})} \tag{4c}$$

A material's resistance to volume change under applied pressure is measured by its bulk modulus (B). $LiHfH_3$ has the largest bulk modulus of 54.34 GPa, as can be shown in Table 6. A crucial metric for determining hardness is the shear modulus (G), which is calculated as the ratio of shear stress to shear strain. Higher values of $LiHfH_3$ indicate stronger resistance to plastic deformation than the other compounds. Young's modulus (Y), which is a crucial indicator of a material's stiffness, is the ratio of tensile stress to strain. A material with a higher Young's modulus (E) estimate will be stiffer; the greatest value of $LiHfH_3$ is 93.99 GPa. Together, these characteristics offer crucial insights into the compound's mechanical behavior. For mechanical characteristics, the following equations are used:

$$\mathrm{A} = \frac{2\mathrm{C_{11}}}{\mathrm{C_{11}} - \mathrm{C_{12}}} \tag{5a}$$

$$\mathrm{Y} = \frac{9\mathrm{GB}}{3\mathrm{B} + \mathrm{G}} \tag{5b}$$

$$\nu = \frac{3B - 2G}{2(2B + G)} \tag{5c}$$

$$\mathrm{H_V} = 0.92\mathrm{k}^{1.137}\mathrm{G}^{0.708} \tag{5(d)}$$

The elastic anisotropy of the cubic $XHfH_3$ compounds was evaluated using the Zener anisotropy factor, $A = 2C_{44}/(C_{11} - C_{12})$. A value of $A = 1$ indicates elastic isotropy, whereas a deviation from unity reflects anisotropic elastic behavior. Based on the

calculated elastic constants, the anisotropy factors are approximately 0.32, 0.48, and 1.23 for $LiHfH_3$, $NaHfH_3$, and $RbHfH_3$, respectively. These values indicate that all three compounds exhibit elastic anisotropy, with $RbHfH_3$ being closest to isotropic behavior among the investigated systems. The lower anisotropy factors for $LiHfH_3$ and $NaHfH_3$ suggest stronger directional dependence in their elastic response, which may influence mechanical durability during hydrogen absorption and desorption cycles.

Hardness of crystalline material, the most widely used empirical formula to estimate Vickers hardness (H_v) in GPa from elastic constant is Tian's model. The formula is sometimes expressed using Pugh's modulus ratio (k = G/B) [65]. Table 6 demonstrates that $LiHfH_3$, with H = 8.36 GPa, is superior to the other materials.

The B/G ratio (Pugh's modulus) is another important factor that determines whether a material is brittle or ductile. According to Pugh's criteria, a B/G ratio of more than 1.75 indicates ductility, whereas a ratio of less than this indicates brittleness. Table 6 B/G ratio shows that $LiHfH_3$ and $NaHfH_3$ are brittle under examination, with the exception of $RbHfH_3$, which has a ductile B/G of 2.05. Moreover, a reliable predictor of the behavior of a material is the Cauchy pressure (C_P), which is equal to $C_{12} - C_{44}$. Brittleness is indicated by a negative C_P value, while ductility is produced by a positive C_P value. It is further shown that $RbHfH_3$ is ductile due to the positive C_P values, but the investigated $LiHfH_3$ and $NaHfH_3$ have brittle features due to the negative values.

Table 6. Calculated elastic parameters: [C11, C12, C44] (GPa), Poisson's ratio (υ), Pugh ratio (B/G), anisotropy factor (A), hardness (Hv), bulk modulus B (GPa), shear modulus G (GPa), and Young's modulus Y (GPa)

Compound	C_{11}	C_{12}	C_{44}	B	G	Y	H_v	υ	B/G	A	C_P
$LiHfH_3$	142.08	10.46	20.76	54.34	38.79	93.99	8.36	0.28	1.40	0.32	-10.30
$NaHfH_3$	127.73	16.01	26.55	53.25	38.27	92.62	8.35	0.29	1.39	0.48	-10.54
$RbHfH_3$	78.59	35.67	26.31	49.97	24.37	62.89	3.91	0.41	2.05	1.23	9.37

The development of hydrogen storage systems relies on the examination of mechanical and anisotropic elastic features. Elastic constants give insight into failure susceptibility, mechanical stability, and resistance to deformation. Directional stress distribution and diffusion behavior, which have a substantial influence on material performance and durability, are illustrated by anisotropy analysis. Thus, computational validation with first-principles elastic simulation offers a viable approach for creating next-generation hydrogen storage material with better long-term stability, safety, and efficiency.

3.4.1 Debye Temperature

Melting temperature and heat capacity are two other material parameters that are closely linked to the Debye temperature (T_D). A higher Debye temperature usually indicates a higher melting point and improved thermal conductivity. The calculated values of the average wave velocity (V_m), longitudinal wave velocity (V_l), transverse wave velocity (V_t), and T_D are shown in Table 7. These equations [47, 48] were used to determine T_D, V_m, V_l, and V_t. Planck's constant (h), the number of atoms per unit cell (n), the Boltzmann constant (k), the density (ρ), the mass of the unit cell atoms (M), and Avogadro's number (Na) are all represented in equation (6).

$$T_D = \frac{h}{k}\left[\frac{3n}{4\pi}\left(\frac{N_a\rho}{M}\right)\right]^{1/3} v_m \tag{6a}$$

Where

$$v_m = \left[\frac{1}{3}\left(\frac{2}{v_l^3} + \frac{1}{v_t^3}\right)\right]^{-1/3} \tag{6b}$$

Exploit the G and B values to get the values of υ_l and υ_t.

$$v_l = \sqrt{\frac{3B + 4G}{\rho}} \quad \text{and} \quad v_t = \sqrt{\frac{G}{\rho}} \tag{6c}$$

The melting temperature (T_m) has also been predicted by using equation (7) [66].

$$T_m\,(K) = [553(K) + 5.911C_{11}] \pm 300 \tag{7}$$

Table 7. The gathered Debye temperature (TD), transverse (υt), longitudinal (υl), and average (υm) wave velocities and melting points (Tm) for $XHfH_3$

Compound	T_D (K)	v_t (m/s)	v_l (m/s)	V_m (m/s)	T_m (K)
$LiHfH_3$	353.69	2731.833	7826.622	3105.163	1389.84 ± 300
$NaHfH_3$	361.54	2689.430	7689.273	3056.981	1308.01 ± 300
$RbHfH_3$	272.51	2031.16	6471.539	2313.463	1017.54 ± 300

From Table 7, it is clear that a greater Debye temperature results in a greater average velocity of sound in the compound. We also observe from Table 7 that the compound $LiHfH_3$ has a greater melting temperature.

Systematic differences in lattice stiffness, bond strength, and thermal stability are revealed by the Debye temperature research in $LiHfH_3$, $NaHfH_3$, and $RbHfH_3$ across the alkali range [67]. Stronger bond and longer structure durability are related to higher Debye temperature, while softer lattices that may improve hydrogen mobility but sacrifice mechanical integrity are suggested by lower values [68]. Debye temperatures are thus a significant component in assessing whether hydrogen storage compounds are acceptable for long-term, practical energy application.

3.5 Optical Properties

Figure. 7 depicts optical properties of the hydride perovskite $LiHfH_3$, $NaHfH_3$, and $RbHfH_3$ as a function of photon energy. The optical responses examined include: (a) real part of the dielectric function $\varepsilon_r(\omega)$; (b) imaginary part $\varepsilon_i(\omega)$; (c) refractive index $n(\omega)$; (d) extinction coefficient $k(\omega)$; (e) real part of the optical conductivity $\sigma_r(\omega)$; (f) imaginary part $\sigma_i(\omega)$; (g) reflectivity $R(\omega)$; (h) absorption coefficient $\alpha(\omega)$; and (i) Electron energy loss $L(\omega)$. Analyzing these parameters provides insight into the suitability of each material for optoelectronic applications. The equation below tells about optical properties.

$$\varepsilon_1(\omega) = 1 + \frac{2}{\pi} P \int_0^{\infty} \frac{\omega' \varepsilon_2(\omega')}{\omega'^2 - \omega^2} d\omega' \tag{8a}$$

$$\varepsilon_2(\omega) = -\frac{2\omega}{\pi} P \int_0^{\infty} \frac{\varepsilon_1(\omega') - 1}{\omega'^2 - \omega^2} d\omega' \tag{8b}$$

The refractive index can be determined by the following equation:

$$\eta\,(\omega) = \left(\frac{\varepsilon_r(\omega)}{2} + \frac{\sqrt{[\varepsilon_r(\omega)]^2 + [\varepsilon_i(\omega)]^2}}{2}\right)^{1/2} \tag{9a}$$

$$\kappa\,(\omega) = \left(\frac{\sqrt{[\varepsilon_r(\omega)]^2 + [\varepsilon_i(\omega)]^2}}{2} - \frac{\varepsilon_r(\omega)}{2}\right)^{1/2} \tag{9b}$$

$$R(\omega) = \frac{n + ik - 1}{n + ik + 1} \tag{10}$$

$$\alpha(\omega) = \frac{4\pi}{\lambda}\kappa\,(\omega) \tag{11}$$

$$L\,(\omega) = \mathrm{Im}\,(\varepsilon(\omega)^{-1}) = \frac{\varepsilon_i(\omega)}{\varepsilon_i{}^2(\omega)} + \varepsilon_i{}^2(\omega) \tag{12}$$

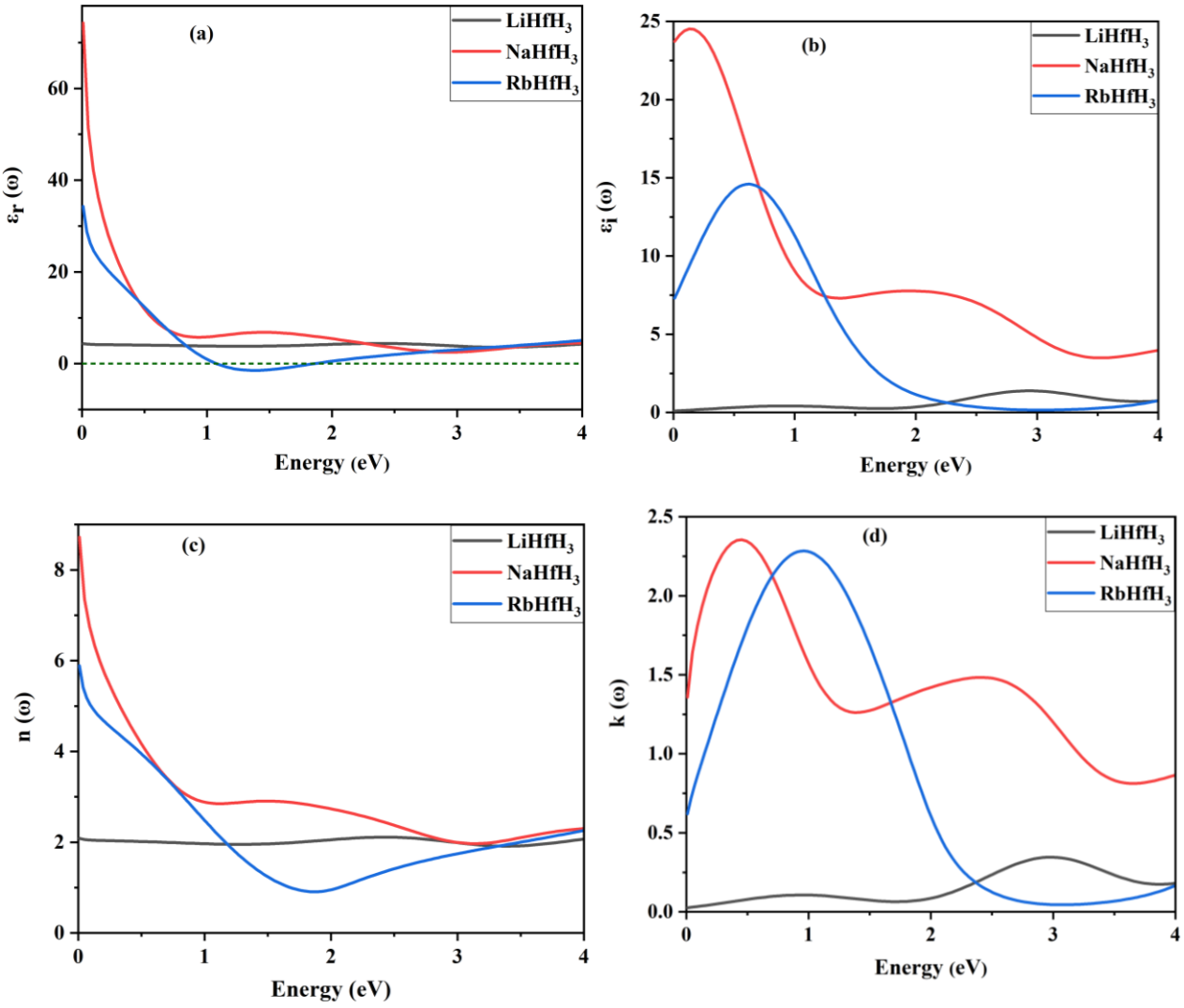

Figure 7. Optical properties of $XHfH_3$ (X = Li, Na, Rb) perovskites as a function of photon energy: (a) (b) real $\varepsilon_r(\omega)$ and imaginary part $\varepsilon_i(\omega)$ of the dielectric function, (c) refractive index n(ω), (d) extinction coefficient k(ω)

In Figure. 7 (a), the real part of the dielectric function, $\varepsilon_r(\omega)$, which indicates the material's polarization responsiveness and energy storage capabilities, varies significantly among the $XHfH_3$ compounds. $NaHfH_3$ has a high static dielectric constant $\varepsilon_r(0)$, followed by $RbHfH_3$. This indicates strong low-frequency electronic polarizability and effective electric-field screening. $LiHfH_3$ has a low frequency-independent $\varepsilon_r(\omega)$, indicating lower polarization effects. As photon energy increases, $\varepsilon_r(\omega)$ for $NaHfH_3$ and $RbHfH_3$ rapidly drops and approaches modest positive values at higher energies, indicating reduced polarization beyond the main interband transition area. $RbHfH_3$ displays a transitory negative $\varepsilon_r(\omega)$ region at ~1.37 to 1.65 eV, indicating plasma-like activity and enhancing reflectivity in this energy range [69]. Overall, the trend $NaHfH_3 > RbHfH_3 > LiHfH_3$ in $\varepsilon_r(0)$ illustrates the considerable effect of alkali metal substitutions on the dielectric response of the $XHfH_3$ system.

In Figure.7 (b), the imaginary portion of the dielectric function, $\varepsilon_i(\omega)$, shows optical absorption arising from interband electronic transitions, displaying a unique energy-dependent pattern for the three compounds. $NaHfH_3$ exhibits a considerably low energy response with a prominent peak at about ~0.18 to 0.3 eV. This predicted a high density of permissible transitions and increased optical activity at low photon energy. $RbHfH_3$ displays a substantial peak at about ~0.68 to 1.0 eV, indicating strong interband transitions in the near infrared range, followed by a fast drop at higher energies. $LiHfH_3$ exhibits a reduced $\varepsilon_i(\omega)$ spanning the spectra, with just a little signature around ~2.93 (approximately 3.0 eV), indicating minimal transition and a larger band gap [70]. Overall, the intensities of $\varepsilon_i(\omega)$ follow the sequence $NaHfH_3 > RbHfH_3 > LiHfH_3$, agreeing with their individual optical absorption trend and emphasizing $NaHfH_3$ as the most optically active molecule among the testing systems.

The refractive index n(ω), displayed in Figure 7 (c), illustrates the energy-dependent refractive index n(ω) of alkali hafnium hydrides $XHfH_3$ in the 0 to 4 eV range, displaying clear composition-dependent optical dispersions [71]. At low photon energies (about 0 eV), $NaHfH_3$ has the largest refractive index, followed by $RbHfH_3$. $LiHfH_3$ has the lowest and nearly constant values ~1.87. It indicates that Na and Rb-based compounds have greater low-energy electronic polarizability than the Li equivalents. As energy increases, the normal dispersion of $RbHfH_3$ falls fast, reaching a minimum at ~1.88 eV [72]. The deeper minimum in $RbHfH_3$ shows reduced interband transition contributions in this energy range, probably related to its greater ionic radius and modified band structure. $LiHfH_3$ displays moderate dispersion across the spectrum, indicating a consistent optical response and fewer low-energy electronic transitions. Beyond ~3 eV, the three compound refractive indices converge to identical value ~2.0 to 2.2, demonstrating comparable high energy optical behavior caused by cores electronic transitions [73]. At low energies, the trend $NaHfH_3 > RbHfH_3 > LiHfH_3$ underscores the relevance of the alkali metal in controlling the optical response of $XHfH_3$, which is critical for optoelectronic and photonic material designs [74].

In Figure. 7 (d) The extinction coefficient, k(ω), describes the attenuation of electromagnetic waves within a material owing to absorptions. $NaHfH_3$ has the greatest k(ω) in the low to mid energy ranges, with a peak approximately at 0.46 eV and a secondary feature nears ~2.5 eV. This suggests high light matter interaction and effective absorption in the visible and near infrared region. $RbHfH_3$ has a significant peak at ~0.95 eV, followed by a fast decrease, show substantial absorption in the near-infrared region [75]. $LiHfH_3$ exhibits a smaller k(ω), with just mild peaks at 3.0 eV, indicating weak absorptions and a larger optical band gap. Overall, the amplitude and position of the peak coincide with the electronic structural and interband transition, following the pattern $NaHfH_3 > RbHfH_3 > LiHfH_3$, commensurate with their respective optical absorption quality [76].

In Figure 8 (e), the $\alpha_r(\omega)$ of $XHfH_3$ (X = Li, Na, Rb) demonstrates the absorptive response associated with permissible electronic transitions. At low photon energy, all compounds exhibit a progressive rise in conductivity, suggesting the beginning of interband transitions. $NaHfH_3$ has the best conductivity over the energy range, with distinct peaks ~0.6 to 1.0 eV and ~2 to 3 eV, indicating substantial optical absorption and increased carrier mobility. $RbHfH_3$ has a peak at ~1 eV, followed by a quick decline, indicating dominant low-energy interband transitions and limited higher energy absorption. $LiHfH_3$ has low conductivity, with a minor increase near ~3 eV, indicating minimal optical absorption. The systematic variation shows that the alkali metal cation has an enormous impact on the true optical conductivity and absorption strength of $XHfH_3$. $NaHfH_3$ has the strongest optoelectronic response.

The imaginary Figure 8 (f) fraction of the optical conductivity $\alpha_i(\omega)$ of $XHfH_3$ (X = Li, Na, Rb) reflects the materials' reactive and dispersive electronic response. Negative α_i values in the low-energy band 0, about 3 eV, show capacitive behavior driven by bound electron polarization. A negative minimum in the middle range ~4.8 about 5.99 eV is caused by substantial interband transitions, with $LiHfH_3$ and $NaHfH_3$ displaying greater responses than $RbHfH_3$. The zero crossover at ~6 (6.5 eV) suggested a resonance or plasma-associated transitions from capacitive to inductive behavior. At larger energies >6.5 eV, α_i turns positive due to more powerful electronic stimulations, with $NaHfH_3$ having the highest dispersions. These findings reveal that alkali metal species successfully influence the optical dispersions and imaginary conductivity of $XHfH_3$.

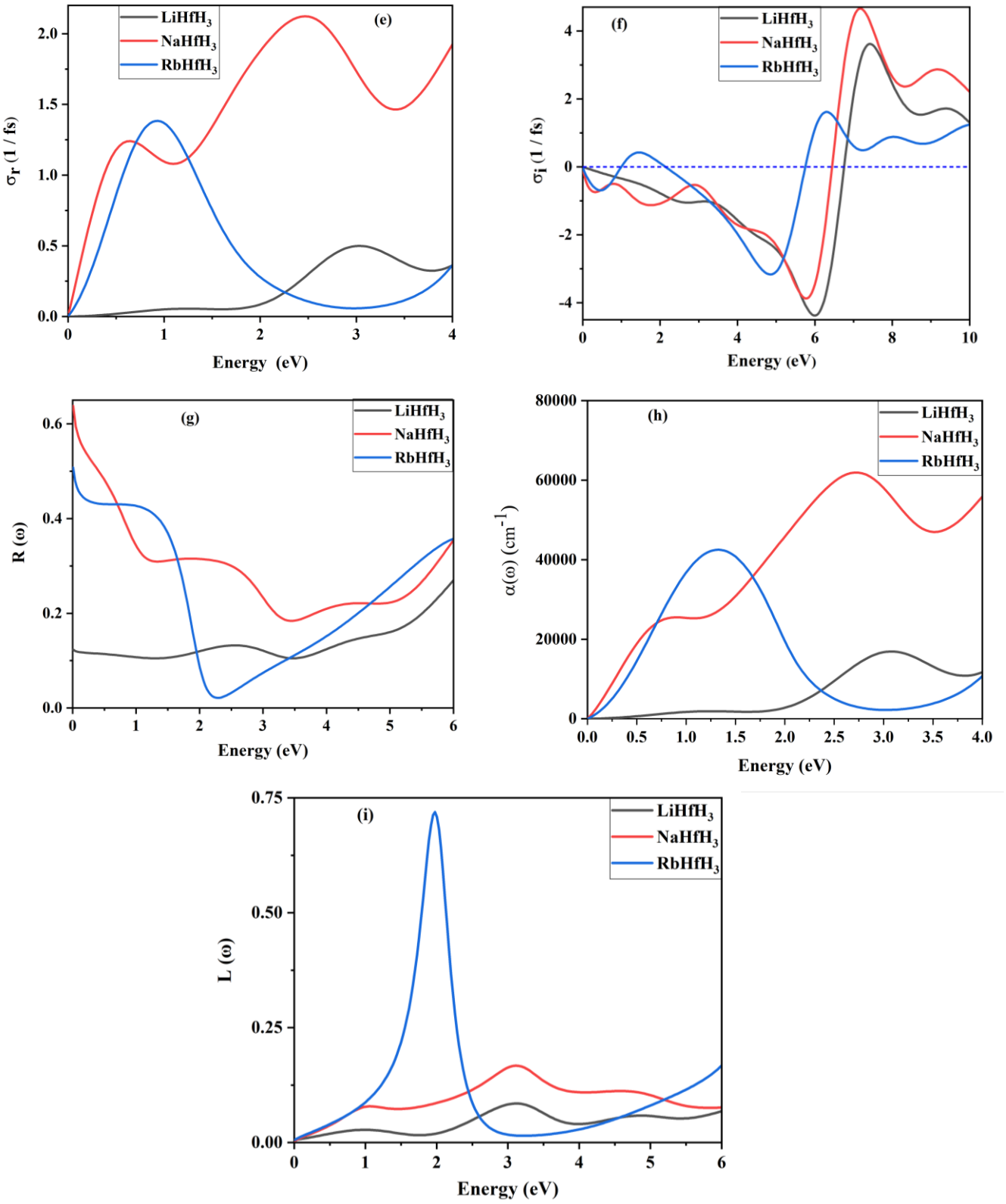

Figure 8. (e) real optical conductivity $\sigma_r(\omega)$, (f) imaginary optical conductivity $\sigma_i(\omega)$, (g) reflectivity $R(\omega)$, (h) absorption coefficient $\alpha(\omega)$, and (i) electron energy loss function $L(\omega)$

Reflectivity R(ω), displayed in Figure 8 (g), of $XHfH_3$ (X = Li, Na, Rb) illustrates the material's response to incoming electromagnetic radiation. All compounds display high reflectivity at low energies <1 eV, suggesting strong metallic or free carrier screenings. $NaHfH_3$ exhibits the greatest reflectivity throughout much of the investigating range, with increasing reductions and a significant dip around ~1.32 and 3.44 eV, which correspond to interband transitions. $RbHfH_3$ has a substantial drop around ~2.28, implying a decrease in reflectivity owing to optical absorptions. $LiHfH_3$ retains a low and generally flat reflectance throughout, suggesting poorer optical sensitivity. Overall, the result demonstrated that the reflectivity and light screening behavior of $XHfH_3$ are substantially influenced by the alkali metal cations. $NaHfH_3$ exhibits the greatest reflecting quality [53].

Figure 8 (h) shows the unique compound-dependent optical responses of the absorption coefficient α(ω) as a function of photon energies. $LiHfH_3$ shows modest absorption in the low energy region, with a delayed commencement and a minor peak approximately 3.05 eV (~1.6×10^4 cm^{-1}), resulting to a considerably higher optical band gap and fewer interband transitions in the visible range. While $NaHfH_3$ displays high and wide absorption from low energies, extending toward a maximum of around ~2.72 eV (~6.2×10^4 cm^{-1}), indicating a better electronic transition with enhanced light-harvesting capabilities. $RbHfH_3$ displays intermediate behavior, reflecting high absorption at around 1.31 eV (4.2×10^4 cm^{-1}), followed by a quick decline, demonstrating low-energy interband transitions. The absorbing strength appears in the corresponding order: $NaHfH_3$ > $RbHfH_3$ > $LiHfH_3$. Thus, $NaHfH_3$ represents the most promising choice among the three compounds examined, especially for optoelectronic and photovoltaic applications in the visible light spectrum.

Figure 8 (i) shows the energy-dependent loss function L(ω) of $XHfH_3$ (X = Li, Na, Rb), which explains the electrical stimulation and plasmon energy loss. All systems show negligible loss at low energies <1 eV, indicating moderate electron damping and the lack of low-energy plasmon modes. $RbHfH_3$ shows a pronounced peak around ~2.67 eV, suggesting a substantial bulk plasmon resonance and increased collective oscillations of charge carriers. However, $NaHfH_3$ exhibits a bigger and less strong maximum near ~2.78 eV, whereas $LiHfH_3$ has weak and smooth characteristics throughout the energy ranges, indicating weaker plasmonic activity. Higher energy >3 eV produced a gradual variation in L(ω) owing to interband electronic transition. The kind of alkali metal cations has a considerable influence on the plasmon resonance strength, peak locations, and energy loss behavior of $XHfH_3$, exhibiting their flexible plasmonic capability.

While optical properties do not directly determine gravimetric hydrogen capacity, they are intrinsically linked to the electronic structure, which governs hydrogen binding strength, hydride phase stability, and diffusion kinetics. Consequently, analysis of the optical response provides a non-destructive and valuable indirect probe of a material's suitability for hydrogen storage, offering insight into its potential performance prior to undertaking more complex and experimentally demanding gas adsorption studies [77-79].

3.6 Phonon Properties

The lattice thermodynamic resilience of these hydrides has been considerably established by the simulated phonon dispersion curve of $XHfH_3$ (X = Li, Na, and Rb) along the high-symmetry orientations X–R–M–G–R in Figure 9. The appearance of soft phonon modes with modest imaginary frequency near the G point and along specific symmetry pathways for $LiHfH_3$ and $NaHfH_3$ implies marginal dynamical instability, which may be offspring by temperature-induced phase transitions or lattice distortion.

The phonon dispersion results indicate that $RbHfH_3$ exhibits no imaginary frequencies across the Brillouin zone, confirming its dynamical stability. In contrast, $LiHfH_3$ and $NaHfH_3$ show imaginary phonon modes, which are signatures of lattice instabilities and suggest that these structures may undergo spontaneous distortions toward lower-energy configurations.

From a practical hydrogen storage perspective, this distinction is critical. Dynamical stability implies that $RbHfH_3$ can maintain its crystal structure under small perturbations, making it a more reliable candidate for reversible hydrogen storage. On the other hand, the presence of soft modes in $LiHfH_3$ and $NaHfH_3$ indicates that these materials may: (i) transform into more stable (possibly unknown) phases, (ii) exhibit structural degradation during hydrogen absorption/desorption cycles, or (iii) require finite temperature or pressure to stabilize dynamically.

The origin of these stability differences can be attributed primarily to ionic size effects and lattice tolerance. The larger ionic radius of Rb^+ leads to an expanded lattice and improved accommodation of hydrogen atoms, reducing internal strain and suppressing lattice instabilities. In contrast, the smaller Li^+ and Na^+ ions result in a more compressed lattice, enhancing H-H and H-metal interactions that can destabilize vibrational modes and produce imaginary frequencies. Additionally, differences in bonding characteristics and mass effects contribute to this behavior. The heavier Rb atom lowers vibrational frequencies and stabilizes lattice dynamics, whereas lighter Li and Na systems tend to exhibit higher vibrational sensitivity and anharmonic effects, which can promote instability [80]. Comprehending phonons improves the optimization of these materials for safe and efficient hydrogen storage.

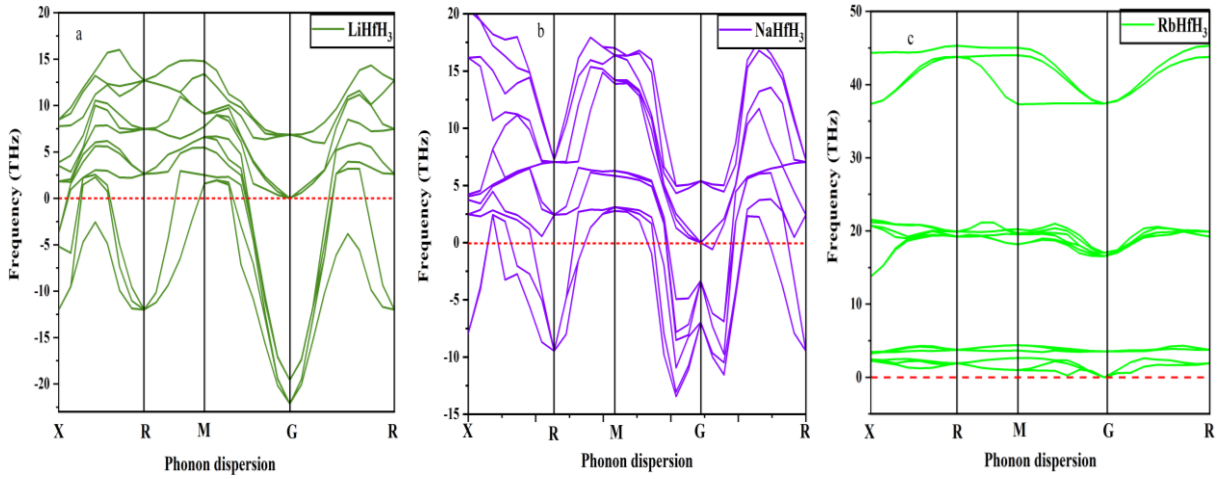

Figure 9. Phonon dispersion relations of $XHfH_3$ (X = Li, Na, Rb), revealing stable dynamics in $RbHfH_3$ and soft modes in Li/Na phases.

Determine temperature-dependent thermodynamic characteristics of the crystallized phase derived from phonon-based density functional theory (DFT) computation inside the harmonic (or quasi-harmonic) approaches. In Figure 10, the information ranges from 0 to 1000 K and contains the enthalpy (H), the entropic contribution (T·S), heat capacity (C_v), and free energy (F or G), which jointly explain the thermal sensitivity and phase stability of the materials. With rising temperature, the enthalpy grows monotonically from 0.00 eV at 0 K to 0.32 eV at 1000 K, indicating the increase in lattice vibrational energy owing to greater atomic displacements from the neutral position [81]. The T·S term demonstrates the same numerical pattern, growing in exact correlation with enthalpy over the whole temperature range. This perfect equality shows that the reported numbers represent solely thermal vibrational donation linked to the 0 K ground state, and presumably omit zero-point energy (ZPE); inclusion of ZPE would result in a limited positive enthalpy at absolute zero. The heat capacity grows gradually from zero at 0 K, consistent with the lack of thermally activated phonon methods, to larger values at rising temperatures, nearing the traditional Dulong-Petit limits when vibrational modes become completely filled [82]. The lack of irregularity or abrupt shifts in C_v suggests that no structural phase shifts, magnetic ordering change, or lattice instabilities occur within the examined temperature interval. The free energy displayed a non-monotonic pattern, falling from 0.00 eV at 0 K to a minimal value around intermediate temperatures (about 200 K), followed by a steady rise toward higher temperature [83, 84]. This inclined trend highlight the opposing effects of inner energy and the entropy the vibrational entropy maintains the phase at low temperature, but at higher temperatures the thermodynamic reason for stability decreases, potentially indicating the appearance of opposing phase or thermal breakdown beyond the study ranges [85]. Meanwhile, the result demonstrates dynamical stability throughout the complete temperature interval while showing the greatest thermodynamic favorability at middle temperatures. The precise numerical consistency between H and T·S across the dataset further implied that the computation represents relative thermal contributions rather than absolute free energy encompassing completed quantum nuclear effects [86].

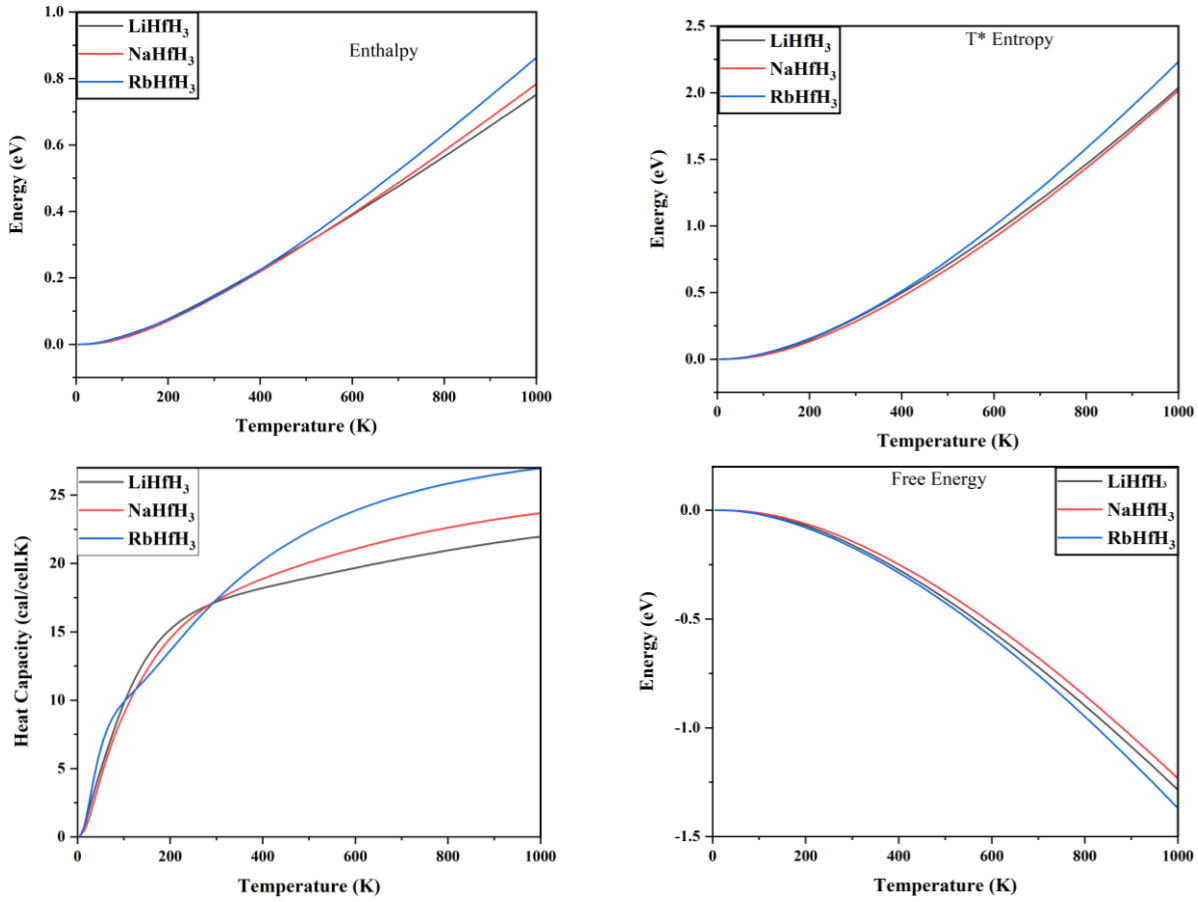

Figure 10. Based on phonon estimation, the temperature-varied Helmholtz free energy, enthalpy, T* entropy, and heat capacity of $XHfH_3$

Regarding the analysis of the potential of hydrides $XHfH_3$ in hydrogen storage applications, their thermodynamic parameters, such as enthalpy, entropy, heat capacity, and free energy, are crucial. These parameters determine how effectively hydrogen is absorbed and released; processes with lower enthalpy and free energy are more energy-efficient. Heat capacity offers information on energy demand for temperature control, while entropy change serves to assess the material thermodynamic favorability. Knowing these qualities makes it possible to select the optimal material, which helps design hydrogen storage systems that are both inexpensive and energy efficient [87, 88].

3.6.1 Debye Temperature

A temperature dependence of the Debye temperatures (T_D), which are a stand-in for lattice rigidity and vibrational frequency, is represented in Figure 11 for the perovskite-type hydrides $LiHfH_3$, $NaHfH_3$, and $RbHfH_3$. The observed rise in (T_D) with increasing ambient temperature suggests that these materials depart from the ideal Debye model, possibly due to harmonic lattice effects and the influence of high-frequency optical phonon modes from the hydrogen atom. A definite pattern develops depending on the atomic mass of the alkali: metal $LiHfH_3$ (containing the lightest element, Li) shows the highest Debye temperature and steepest slope, signifying the strongest interatomic bonding and best thermal stability.

The heaviest element, Rb, is present in $RbHfH_3$, which exhibits the lowest (TD) values and a propensity to plateau, indicating a "softer" lattice with fewer vibrational modes. The shift from the low-temperature limit to the intermediate regime, when lattice expansion started to affect the effective vibrational cutoff, is characterized by the dramatic decrease near 0 K.

An essential aspect in evaluating whether metal hydrides $XHfH_3$ are appropriate for storing hydrogen is their Debye temperatures. Better thermal stability, which is important for efficient hydrogen absorption and desorption over a temperature range, is indicated by a higher Debye temperature. $LiHfH_3$ is a feasible alternative for hydrogen storage because it has the largest Debye temperature of the materials investigated, suggesting that it is more stable at higher temperatures. However, because of their lower Debye temperature, $RbHfH_3$ and $NaHfH_3$ may not be as well-suited for high-temperature applications. $LiHfH_3$ is thus probably the most efficient choice for storing hydrogen, although the optimal materials selection also demands consideration of another thermodynamic factor [22, 89, 90].

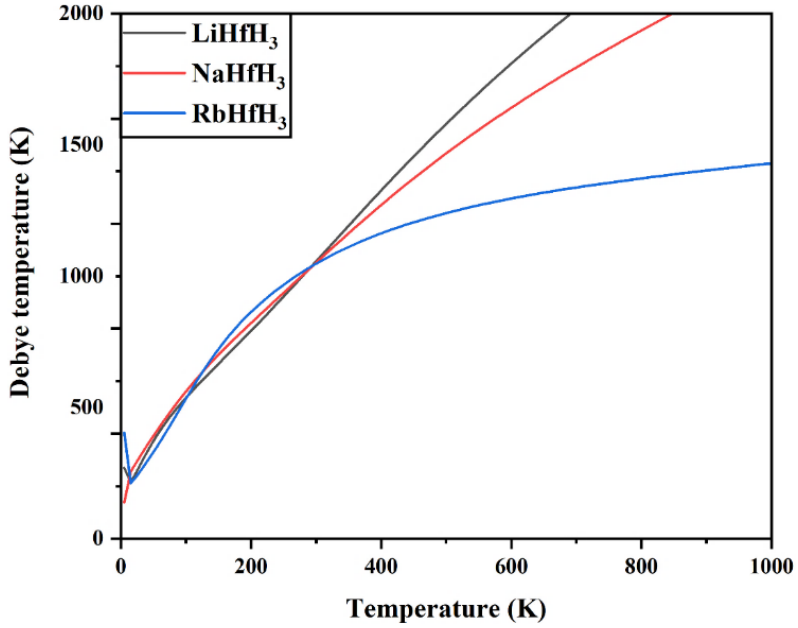

Figure 11. Variation of Debye temperature with temperature for $XHfH_3$

4. Conclusions

In this work, the structural, electronic, magnetic, mechanical, phonon, thermal, optical, and hydrogen-storage-related properties of $XHfH_3$ (X = Li, Na, and Rb) perovskite hydrides were investigated using first-principles calculations, supported by classical molecular dynamics simulations. The optimized lattice parameters increase from $LiHfH_3$ to $RbHfH_3$, consistent with the increasing ionic radius of the alkali-metal cation. Negative formation energies indicate thermodynamic stability of the investigated compounds, while the calculated elastic constants satisfy the Born stability criteria, confirming their mechanical stability under the considered conditions. Electronic band-structure and density-of-states analyses reveal metallic behavior for all three compounds. Spin-polarized calculations show that $LiHfH_3$ relaxes to an essentially non-magnetic state, whereas $NaHfH_3$ and $RbHfH_3$ retain finite magnetic moments of approximately 2.05 μB and 2.08 μB, respectively. This suggests that alkali-site substitution and lattice expansion can influence spin polarization in hafnium-based hydride perovskites. Phonon dispersion analysis indicates dynamic stability for $RbHfH_3$, while $LiHfH_3$ and $NaHfH_3$ exhibit imaginary phonon modes, suggesting lattice instabilities that should be considered in future experimental or computational studies. The calculated gravimetric hydrogen-storage capacities are 1.61 wt.% for $LiHfH_3$, 1.48 wt.% for $NaHfH_3$, and 1.13 wt.% for $RbHfH_3$. Although these values confirm the hydrogen-containing nature of the compounds, they remain modest compared with practical hydrogen-storage targets. In addition, the predicted desorption temperatures are high, indicating that these materials are unlikely to be directly suitable for practical reversible hydrogen storage without further modification. Nevertheless, the observed trends in bonding, magnetism, phonon stability, and thermal behavior provide useful fundamental insight into alkali-metal effects in $XHfH_3$ hydride perovskites. Future work should focus on compositional tuning, defect engineering, catalytic modification, and experimental validation to determine whether the desorption behavior and lattice stability can be improved.

Author Contributions

Investigation; Conceptualization; Software; Writing- Original Draft Preparation, N. A. and S. Z. U.; Validation, Formal Analysis, D.R. and M. A.; Visualization, Writing- Review & Editing, M.u.R, A.J., and M. Y. A.; Supervision, S. Z. U. and D. R. All authors have read and agreed to the published version of the manuscript.

Conflict of Interest

The author declares no conflict of interest related to the publication of this research.

Data Availability Statement

The data that support the findings of this study are available from the corresponding author upon reasonable request.

Funding Declaration

The authors would like to clarify that no external funds or financial supports was received for the research.

Acknowledgments

The author extends their gratitude to Govt. Postgraduate College Kohat for theirs support and the Higher Education Department for their assistance and resources.

References

[1] A. Yakymchuk, B. Baran-Zgłobicka, and R. M. Woruba, "Advanced Energy Collection and Storage Systems: Socio-Economic Benefits and Environmental Effects in the Context of Energy System Transformation," Energies, 19, 2026]. https://doi.org/10.3390/en19020309

[2] D. Adu, D. Jianguo, S. N. Asomani, and A. J. E. R. Abbey, "Energy generation and carbon dioxide emission-The role of renewable energy for green development," vol. 12, pp. 1420-1430, 2024. https://doi.org/10.1016/j.egyr.2024.07.013

[3] A. S. Mekonnin, K. Wacławiak, M. Humayun, S. Zhang, and H. Ullah, "Hydrogen Storage Technology, and Its Challenges: A Review," Catalysts, 15, 2025]. https://doi.org/10.3390/catal15030260

[4] B. A. Alqahtani, H. Zentou, M. M. Abdelnaby, and M. N. J. T. C. R. Shaikh, "Hydrogen: Challenges and Opportunities for Storage and Transportation in the Clean Energy Economy," vol. 26, no. 2, pp. e202500218, 2026. https://doi.org/10.1002/tcr.202500218

[5] S. Eom, S. Kim, G. Han, and S. J. E. Lee, "Low-cost green hydrogen from renewable energy curtailment: A techno-economic analysis with a real-time AI-driven approach," pp. 140569, 2026. https://doi.org/10.1016/j.energy.2026.140569

[6] M.-H. Kuo, N. Neykova, and I. Stachiv, "Overview of the Recent Findings in the Perovskite-Type Structures Used for Solar Cells and Hydrogen Storage," Energies, vol. 17, no. 18, pp. 4755, 2024. https://doi.org/10.3390/en17184755

[7] T. Dakhil, H. Hamidinezhad, and A. S. J. O. M. Baron, "Fabrication and characterization of a hybrid organic-inorganic perovskite materials and applications in solar cell," vol. 160, pp. 116708, 2025. https://doi.org/10.1016/j.optmat.2025.116708

[8] A. M. M. Rawashdeh, M. A. Kalili, S. Abu-rajouh, A. J. J. o. M. E. Obeidat, and Performance, "Toward Efficient Hydrogen Storage: Physical and Hydrogen Storage Properties of APdH3 and ARuH3 (A= Na, Ca, Sr) Perovskite Hydrides," pp. 1-13, 2026. https://doi.org/10.1007/s11665-026-13369-1

[9] M. U. Rahman, M. F. Elsadek, R. Roopashree, and A. J. R. i. I. C. Kashyap, "Advancing hydrogen storage and exploring the potential of perovskite hydrides and metal hydrides," no. 0, 2025. https://doi.org/10.1515/revic-2025-0006

[10] Y. Pan, Z. Li, I. J. R. Jain, and S. E. Reviews, "Recent progress of ABH3 perovskite hydrides for hydrogen storage: Design strategies, challenges and prospects," vol. 234, pp. 116925, 2026. https://doi.org/10.1016/j.rser.2026.116925

[11] A. R. Paul, S. Mehla, and S. Bhargava, "Intermetallic compounds for hydrogen storage: Current status and future perspectives," Small, vol. 21, no. 14, pp. 2408889, 2025. https://doi.org/10.1002/smll.202408889

[12] S. Srivastava, "Hydrogen storage materials for vehicular applications," Energy Storage, vol. 6, no. 1, pp. e524, 2024. https://doi.org/10.1002/est2.524

[13] R. Song, Y. Chen, S. Chen, N. Xu, and W. Zhang, "First-principles to explore the hydrogen storage properties of XPtH3 (X= Li, Na, K, Rb) perovskite type hydrides," International Journal of Hydrogen Energy, vol. 57, pp. 949-957, 2024. https://doi.org/10.1016/j.ijhydene.2024.01.116

[14] M. A. Jawad, and S. S. A. Gillani, "First-principles computation of hydrides-perovskites XZrH3 (X= Ba, Ca, and Sr): evaluation of structural, electronic, optical and mechanical properties for hydrogen storage," The European Physical Journal Applied Physics, vol. 99, pp. 25, 2024. https://doi.org/10.1051/epjap/2024240064

[15] J. Zhou, S. Zhang, R. Song, S. Chen, Y. Chen, and J. Hou, "First-principles screening of the physical and hydrogen storage properties of Rh-based perovskites XRhH3 (X= Ca, Ba) for hydrogen storage applications," Physica Scripta, vol. 100, no. 8, pp. 0859a6, 2025. https://doi.org/10.1088/1402-4896/adfba6

[16] M. Boubchir, R. Boubchir, N. M. Belmessaoud, M. Kadous, H. Aourag, and B. Bouhafs, "Coupling DFT with PCA for a comprehensive study of Rb-based 5d transition metal hydride perovskites for hydrogen storage applications," Computational and Theoretical Chemistry, vol. 1255, pp. 115586, 2026/01/01/, 2026. https://doi.org/10.1016/j.comptc.2025.115586

[17] M. Archi, O. Bajjou, k. Rahmani, and B. Elhadadi, "Theoretical DFT insights into the stability, electronic, mechanical, optical, thermodynamic, and hydrogen storage properties of RbXH3 (X = Si, Ge, Sn) Perovskite Hydrides," Materials Research Bulletin, vol. 188, pp. 113434, 2025/08/01/, 2025. https://doi.org/10.1016/j.materresbull.2025.113434

[18] Y. Selmani, H. Labrim, A. Jabar, and L. Bahmad, "Computational study of the mechanical stability, hydrogen storage and optoelectronic properties of new perovskite hydrides CsXH3 (X = Ca, Sr and Ba)," Inorganic Chemistry Communications, vol. 170, pp. 113335, 2024/12/01/, 2024. https://doi.org/10.1016/j.inoche.2024.113335

[19] Q. Zhou, M. Jiang, J. Xu, Z.-H. Xie, and P. J. I. J. o. H. E. Munroe, "Accelerated discovery of hydrogen storage hydride perovskites: A combined machine learning and first-principles approach," vol. 179, pp. 151697, 2025. https://doi.org/10.1016/j.ijhydene.2025.151697

[20] Q. Wang, X. Kong, H. Han, G. Sang, G. Zhang, and T. J. A. S. S. Gao, "Effect of doping Hf on the hydrogen dissociation and diffusion mechanism on the ZrCo (110) surface," vol. 483, pp. 383-390, 2019. https://doi.org/10.1016/j.apsusc.2019.03.316

[21] G. Muradyan, S. Dolukhanyan, O. Ter-Galstyan, N. Mnatsakanyan, S. Khasanov, K. Asatryan, S. Mardanyan, A. J. J. o. A. Hovhannisyan, and Compounds, "The role of hydrogen in the synthesis of High-entropy alloys and their hydrides," vol. 1010, pp. 177327, 2025. https://doi.org/10.1016/j.jallcom.2024.177327

[22] A. Hammad, D. Bezzerga, F. Keramsi, I. Djebablia, M. Zaman, M. Fellah, and E.-A. Haidar, "First principles investigation of hafnium-based perovskite hydrides XHfH3 (X: Li, Na, K, and Rb) for hydrogen storage applications," Fuel, vol. 413, pp. 138149, 2026/06/01/, 2026. https://doi.org/10.1016/j.fuel.2025.138149

[23] N. Marzari, D. Vanderbilt, and M. C. Payne, "Ensemble density-functional theory for ab initio molecular dynamics of metals and finite-temperature insulators," Physical review letters, vol. 79, no. 7, pp. 1337, 1997. https://doi.org/10.1103/PhysRevLett.79.1337

[24] D. Vanderbilt, "Soft self-consistent pseudopotentials in a generalized eigenvalue formalism," Physical review B, vol. 41, no. 11, pp. 7892, 1990. https://doi.org/10.1103/PhysRevB.41.7892

[25] H. Xu, and D. Guan, "Exceptional anisotropic noncovalent interactions in ultrathin nanorods: the terminal σ-hole," ACS Applied Materials & Interfaces, vol. 14, no. 45, pp. 51190-51199, 2022. https://doi.org/10.1021/acsami.2c14041

[26] J. U. Rehman, M. Usman, S. Amjid, M. Sagir, M. B. Tahir, A. Hussain, I. Alam, R. Nazir, H. Alrobei, and S. Ullah, "First-principles calculations to investigate structural, electronics, optical and elastic properties of Sn-based inorganic Halide-perovskites CsSnX3 (X= I, Br, Cl) for solar cell applications," Computational and Theoretical Chemistry, vol. 1209, pp. 113624, 2022. https://doi.org/10.1016/j.comptc.2022.113624

[27] S. Berri, "Ab initio study of fundamental properties of XAlO3 (X= Cs, Rb and K) compounds," Journal of Science: Advanced Materials and Devices, vol. 3, no. 2, pp. 254-261, 2018. https://doi.org/10.1016/j.jsamd.2018.03.001

[28] G. Surucu, A. Gencer, A. Candan, H. H. Gullu, and M. Isik, "CaXH3 (X= Mn, Fe, Co) perovskite-type hydrides for hydrogen storage applications," International Journal of Energy Research, vol. 44, no. 3, pp. 2345-2354, 2020. https://doi.org/10.1002/er.5062

[29] G. P. Li, and I. P. Hamilton, "The HF2−-(H2O)2 complex: a theoretical study," Chemical Physics Letters, vol. 368, no. 1, pp. 236-241, 2003/01/14/, 2003. https://doi.org/10.1016/S0009-2614(02)01853-5

[30] A. Lemnawar, I. Elbakkali, N. Bouri, H. Labrim, S. Amraoui, K. Moussa, M. Louzazni, and K. Nouneh, "First principles study of the physical properties of Y2FeCrO6 double perovskite: Optoelectronic and thermoelectric applications," Results in Engineering, vol. 25, pp. 104530, 03/01, 2025. https://doi.org/10.1016/j.rineng.2025.104530

[31] R. Khalil, S. Hayat, M. Iqbal Hussain, A. Rana, and F. Hussain, "DFT based first principles study of novel combinations of perovskite-type hydrides XGaH 3 (X = Rb, Cs, Fr) for hydrogen storage applications," AIP Advances, vol. 11, pp. 025032, 02/01, 2021. https://doi.org/10.1063/5.0037790

[32] M. Usman, D. Pan, M. K. Masood, and C. Zhang, "Mn-based hydride perovskites XMnH3 (X = K, Li): A DFT study for physical properties, and hydrogen storage capability," Solid State Communications, vol. 390, pp. 115600, 2024/10/15/, 2024. https://doi.org/10.1016/j.ssc.2024.115600

[33] N. Ghaffar, M. Usman, J. Ur Rehman, A. Hussain, S. Mansoor Ali, and M. Ali, "A DFT study to investigate physical properties and hydrogen storage capability of Mn-based hydride perovskites XMnH3 (X = Ba, Ca) for hydrogen storage application," Inorganic Chemistry Communications, vol. 161, pp. 112167, 2024/03/01/, 2024. https://doi.org/10.1016/j.inoche.2024.112167

[34] B. Cullity, Elements of X-ray Diffraction: Hsin Yueh, 1986.

[35] A. R. West, Solid state chemistry and its applications: John Wiley & Sons, 2022.

[36] R. Jenkins, and R. L. Snyder, Introduction to X-ray powder diffractometry: Wiley Online Library, 1996. https://doi.org/10.1002/9781118520994

[37] T. Zelai, "Study of magnetic, thermoelectric, and mechanical properties of double perovskites Be2XH6 (X= Cr and Mn) for spintronic and hydrogen-storage applications," Inorganic Chemistry Communications, vol. 165, pp. 112579, 2024. https://doi.org/10.1016/j.inoche.2024.112579

[38] Y. Song, M. K. Shahzad, S. Hussain, A. Farrukh, M. Riaz, H. Sattar, G. Khan, G. A. Ashraf, S. M. Ali, and M. Alam, "Theoretical prediction of perovskite ARH3 (A= K, Li, Rb; RCa, Sr) hydride materials for hydrogen storage applications: A DFT investigation," International Journal of Hydrogen Energy, vol. 79, pp. 1472-1482, 2024. https://doi.org/10.1016/j.ijhydene.2024.07.069

[39] S. Al, "Mechanical and electronic properties of perovskite hydrides LiCaH 3 and NaCaH 3 for hydrogen storage applications," The European Physical Journal B, vol. 94, no. 9, pp. 182, 2021. https://doi.org/10.1140/epjb/s10051-021-00195-8

[40] M. K. Masood, W. Khan, K. Chaoui, Z. Ashraf, S. Bibi, A. Kanwal, A. A. Alothman, and J. Rehman, "Theoretical investigation of XSnH3 (X: Rb, Cs, and Fr) perovskite hydrides for hydrogen storage application," International Journal of Hydrogen Energy, vol. 63, pp. 1248-1257, 2024. https://doi.org/10.1016/j.ijhydene.2024.03.229

[41] A. Yaqoob, A. Hussain, N. Jabeen, and A. M. Fallatah, "DFT Study of Physical Properties for A2H3X (A= Sr, Ba; X= Cl, Br) Compounds: Their Possible Applications for Hydrogen Storage and Optoelectronic Devices," ChemistrySelect, vol. 10, no. 34, pp. e03422, 2025. https://doi.org/10.1002/slct.202503422

[42] A. Almahmoud, H. Alkhalidi, and A. Obeidat, "First-Principles Investigation of Hydrogen Storage in Novel X_2Feh_5 Hydrides (X= Ca, Mg, Ba)," Available at SSRN 5034496, 2025. https://doi.org/10.2139/ssrn.5034496

[43] G. M. Mustafa, B. Younas, A. K. Alqorashi, S. A. Mahmoud, A. Aljameel, A. A. Alshihri, and Q. Mahmood, "Study of structural, optical, mechanical, thermoelectric, and hydrogen storage properties of CsXH3 (X= Ca, Sr, Ba) hydrides," International Journal of Hydrogen Energy, vol. 92, pp. 938-948, 2024. https://doi.org/10.1016/j.ijhydene.2024.10.245

[44] K. Cousins, and R. Zhang, "Highly Porous Organic Polymers for Hydrogen Fuel Storage," Polymers, vol. 11, no. 4, pp. 690, 2019. https://doi.org/10.3390/polym11040690

[45] M. M. Parvaiz, A. Khalil, A. Hannan, M. B. Tahir, M. A. Assiri, and M. Rafique, "Comprehensive DFT analysis of Cr-based XCrH3 (X= Li, K, Cs) metal hydride perovskites: Unveiling multifaceted properties and hydrogen storage potential," Next Materials, vol. 8, pp. 100559, 2025. https://doi.org/10.1016/j.nxmate.2025.100559

[46] L. Schlapbach, and A. Züttel, "Hydrogen-storage materials for mobile applications," Materials for Sustainable Energy, pp. 265-270. https://doi.org/10.1142/9789814317665_0038

[47] L. Schlapbach, and A. Züttel, "Hydrogen-storage materials for mobile applications," Nature, vol. 414, pp. 353-358, 2001. https://doi.org/10.1038/35104634

[48] F. T. Zohra, C. J. Webb, K. E. Lamb, and E. M. Gray, "Degradation of metal hydrides in hydrogen-based thermodynamic machines: A review," International Journal of Hydrogen Energy, vol. 64, pp. 417-438, 2024/04/25/, 2024. https://doi.org/10.1016/j.ijhydene.2024.03.228

[49] M. U. Rahman, M. F. Elsadek, R. Roopashree, and A. Kashyap, "Advancing hydrogen storage and exploring the potential of perovskite hydrides and metal hydrides," Reviews in Inorganic Chemistry, no. 0, 2025. https://doi.org/10.1515/revic-2025-0006

[50] Y. Zhang, X. Xue, T. He, H. Zhang, S. Zhang, J. Wang, A. Li, and Y. Liu, "A review on advances, strategies, and future perspectives of solid-state hydrogen storage materials," Sustainable Chemistry for Energy Materials, vol. 2, pp. 100014, 2025/12/01/, 2025. https://doi.org/10.1016/j.scenem.2025.100014

[51] F. J. Desai, M. N. Uddin, M. M. Rahman, and R. Asmatulu, "A critical review on improving hydrogen storage properties of metal hydride via nanostructuring and integrating carbonaceous materials," International Journal of Hydrogen Energy, vol. 48, no. 75, pp. 29256-29294, 2023/09/01/, 2023. https://doi.org/10.1016/j.ijhydene.2023.04.029

[52] V. N. Kudiiarov, A. Kenzhiyev, R. R. Elman, N. Kurdyumov, I. A. Ushakov, A. V. Tereshchenko, R. S. Laptev, M. A. Kruglyakov, and P. I. Khomidzoda, "The Defect Structure Evolution in MgH2-EEWNi Composites in Hydrogen Sorption-Desorption Processes," Metals, 15, 2025]. https://doi.org/10.3390/met15010072

[53] T. C.-J. Yang, P. Fiala, Q. Jeangros, and C. Ballif, "High-bandgap perovskite materials for multijunction solar cells," Joule, vol. 2, no. 8, pp. 1421-1436, 2018. https://doi.org/10.1016/j.joule.2018.05.008

[54] Q. Sun, P. Jena, Q. Wang, and M. Marquez, "First-principles study of hydrogen storage on Li12C60," J Am Chem Soc, vol. 128, no. 30, pp. 9741-5, Aug 2, 2006. https://doi.org/10.1021/ja058330c

[55] H. Murtaza, A. B. M. Ibrahim, J. Munir, A. Kumar, M. A. Habib, A. D. Oza, and Q. Ain, "Excellent hydrogen storage capabilities and optoelectronic attributes of XClH6 (Li, Na, and K) perovskite hydrides for green energy technologies," RSC Advances, vol. 15, no. 38, pp. 31609-31619, 2025. https://doi.org/10.1039/D5RA03544A

[56] P. Dang, Epitaxial Spin-Orbit and Magnetic Materials for Integration onto a Semiconductor Platform: Cornell University, 2021.

[57] S. Ding, X. Yan, A. Bergara, X. Zhang, Y. Liu, and G. Yang, "Supporting Information for Intrinsic ferromagnetism in 2D Fe2H with a high Curie temperature," 2022. https://doi.org/10.1021/acsami.2c10504

[58] Q. Wu, Y. Zhang, Q. Zhou, J. Wang, and X. C. Zeng, "Transition-metal dihydride monolayers: a new family of two-dimensional ferromagnetic materials with intrinsic room-temperature half-metallicity," The Journal of Physical Chemistry Letters, vol. 9, no. 15, pp. 4260-4266, 2018. https://doi.org/10.1021/acs.jpclett.8b01976

[59] L. Ji, J. W. Chen, Z. G. Zheng, Z. G. Qiu, S. Y. Peng, S. H. Zhou, and D. C. Zeng, "Excellent degradation performance of the Fe78Si11B9P2 metallic glass in azo dye treatment," Journal of Physics and Chemistry of Solids, vol. 145, pp. 109546, 2020/10/01/, 2020. https://doi.org/10.1016/j.jpcs.2020.109546

[60] M. Born, "On the stability of crystal lattices. I." pp. 160-172. https://doi.org/10.1017/S0305004100017138

[61] F. Mouhat, and F.-X. Coudert, "Necessary and sufficient elastic stability conditions in various crystal systems," Physical review B, vol. 90, no. 22, pp. 224104, 2014. https://doi.org/10.1103/PhysRevB.90.224104

[62] W. Voigt, and W. Voigt, Wechselbeziehungen zwischen zwei Tensortripeln.(Elastizität und innere Reibung.): Springer, 1966. https://doi.org/10.1007/978-3-663-15884-4_8

[63] R. S. Crosson, and J. W. Lin, "Voigt and Reuss prediction of anisotropic elasticity of dunite," Journal of Geophysical Research, vol. 76, no. 2, pp. 570-578, 1971. https://doi.org/10.1029/JB076i002p00570

[64] R. Hill, "The elastic behaviour of a crystalline aggregate," Proceedings of the Physical Society. Section A, vol. 65, no. 5, pp. 349, 1952. https://doi.org/10.1088/0370-1298/65/5/307

[65] Y. Liu, C. Fang, S. Lin, G. Liu, B. Zhang, H. Shi, N. Dong, N. Yang, F. Zhang, and X. Guo, "Calculation of mechanical properties, electronic structure and optical properties of CsPbX3 (X= F, Cl, Br, I)," Molecules, vol. 28, no. 22, pp. 7643, 2023. https://doi.org/10.3390/molecules28227643

[66] M. Sanati, R. Albers, T. Lookman, and A. Saxena, "Elastic constants, phonon density of states, and thermal properties of UO 2," Physical Review B-Condensed Matter and Materials Physics, vol. 84, no. 1, pp. 014116, 2011. https://doi.org/10.1103/PhysRevB.84.014116

[67] P. Debye, "Zur theorie der spezifischen wärmen," Annalen der Physik, vol. 344, no. 14, pp. 789-839, 1912. https://doi.org/10.1002/andp.19123441404

[68] O. L. Anderson, "A simplified method for calculating the Debye temperature from elastic constants," Journal of Physics and Chemistry of Solids, vol. 24, no. 7, pp. 909-917, 1963. https://doi.org/10.1016/0022-3697(63)90067-2

[69] A. Almahmoud, H. Alkhalidi, and A. Obeidat, "Comprehensive DFT analysis of structural, mechanical, electronic, optical, and hydrogen storage properties of novel perovskite-type hydrides Y_2CoH_6 (YCa, Ba, Mg, Sr)," Journal of Energy Storage, vol. 117, pp. 116146, 2025. https://doi.org/10.1016/j.est.2025.116146

[70] M. Zaman, M. Rehman, I. Zeba, S. Zafar, and S. Gillani, "Optimised structural, electronic, optical and mechanical properties of SrTiO3-xHx for photovoltaic applications: a DFT insight," Molecular Physics, vol. 123, no. 11, pp. e2410483, 2025. https://doi.org/10.1080/00268976.2024.2410483

[71] S. Fatima, M. Rizwan, H. M. N. Ullah, S. S. Ali, H. Naeem, and Z. Usman, "Efficient hydrogen storage in KCaF3 using GGA and HSE approach," International Journal of Hydrogen Energy, vol. 48, no. 9, pp. 3566-3582, 2023. https://doi.org/10.1016/j.ijhydene.2022.10.187

[72] N. Ghaffar, M. Usman, J. U. Rehman, A. Hussain, S. M. Ali, and M. Ali, "A DFT study to investigate physical properties and hydrogen storage capability of Mn-based hydride perovskites XMnH3 (X= Ba, Ca) for hydrogen storage application," Inorganic Chemistry Communications, vol. 161, pp. 112167, 2024. https://doi.org/10.1016/j.inoche.2024.112167

[73] M. U. Ghani, M. Sagir, M. B. Tahir, S. Ullah, and M. A. Assiri, "An extensive study of structural, electronic, elastic, mechanical and optical properties of XCdH3 (X= K, Rb) for hydrogen storage applications: first-principles approach," International Journal of Hydrogen Energy, vol. 55, pp. 1265-1272, 2024. https://doi.org/10.1016/j.ijhydene.2023.11.199

[74] M. Morsi, G. Asnag, A. S. Assran, R. Alwafi, A. Tarabiah, N. A. Alshehri, A. N. Al-Hakimi, and A. Saeed, "Reinforced PEO/Cs polymers blend with Al2O3/TiO2 hybrid nanofillers: nanocomposites for optoelectronics and energy storage," Journal of Energy Storage, vol. 88, pp. 111554, 2024. https://doi.org/10.1016/j.est.2024.111554

[75] M. Zaman, S. Zafar, I. Zeba, and S. Gillani, "DFT assessment of KBeO3-xHx perovskites: Revealing ion substitution mechanisms for enhanced solid hydrogen storage," International Journal of Hydrogen Energy, vol. 138, pp. 307-319, 2025. https://doi.org/10.1016/j.ijhydene.2025.05.126

[76] S. Zafar, R. Fatima, S. Gillani, M. Zaman, B. Ahmad, and D. Akhtar, "Novel MgBH3 (B= Al, Si, P, S) perovskites predicted via DFT for high-performance solid hydrogen systems," Materials Today Physics, pp. 101815, 2025. https://doi.org/10.1016/j.mtphys.2025.101815

[77] J. Reilly, and R. Wiswall, "Formation and properties of iron titanium hydride," Inorganic Chemistry, vol. 13, no. 1, pp. 218-222, 1974. https://doi.org/10.1021/ic50131a042

[78] A. Züttel, "Materials for hydrogen storage," Materials today, vol. 6, no. 9, pp. 24-33, 2003. https://doi.org/10.1016/S1369-7021(03)00922-2

[79] P. Chen, Z. Xiong, J. Luo, J. Lin, and K. L. Tan, "Interaction of hydrogen with metal nitrides and imides," Nature, vol. 420, no. 6913, pp. 302-304, 2002. https://doi.org/10.1038/nature01210

[80] L. Boeri, "Understanding novel superconductors with ab initio calculations," Handbook of Materials Modeling: Applications: Current and Emerging Materials, pp. 73-112: Springer, 2020. https://doi.org/10.1007/978-3-319-44680-6_21

[81] L. Yang, Y. Cao, Z. Xu, and N. Qu, "First-principles prediction of hydrogen storage capabilities in Pd-based alkali metal hydride X2PdH4 (X = Na, K, Rb, and Cs)," International Journal of Hydrogen Energy, vol. 100, pp. 444-455, 2025/01/27/, 2025. https://doi.org/10.1016/j.ijhydene.2024.12.318

[82] L. Yang, Y. Cao, Z. Xu, and N. Qu, "First-principles prediction of hydrogen storage capabilities in Pd-based alkali metal hydride X2PdH4 (X= Na, K, Rb, and Cs)," International Journal of Hydrogen Energy, vol. 100, pp. 444-455, 2025. https://doi.org/10.1016/j.ijhydene.2024.12.318

[83] Z. ur Rehman, M. A. Rehman, B. Rehman, M. Amjad, M. Awais, I. Iqbal, and A. Rafique, "A DFT study of structural, electronic, mechanical, phonon, thermodynamic, and H2 storage properties of lead-free perovskite hydride MgXH3 (X= Cr, Fe, Mn)," Journal of Physics and Chemistry of Solids, vol. 186, pp. 111801, 2024. https://doi.org/10.1016/j.jpcs.2023.111801

[84] Y. He, J. Du, S.-m. Liu, C. Tian, M. Zhang, Y.-h. Zhu, H.-x. Zhong, X. Wang, and J.-j. Shi, "Metal-bonded perovskite lead hydride with phonon-mediated superconductivity exceeding 46 K under ambient pressure," Journal of Physics: Condensed Matter, vol. 36, no. 20, pp. 205502, 2024. https://doi.org/10.1088/1361-648X/ad2806

[85] M. A. Rahman, and A. A. Hossain, "Investigating the physical and hydrogen storage properties of alkali metal-based cobalt hydrides," International Journal of Hydrogen Energy, vol. 97, pp. 457-468, 2025. https://doi.org/10.1016/j.ijhydene.2024.11.441

[86] Z. Zang, X. Lu, A. Hussain, M. K. Shahzad, S. Hussain, A. Kumar, M. M. Rekha, B. Pattanayak, V. Tirth, and M. Hussien, "Study of structural, electronic, phonon, thermodynamic, and hydrogen storage properties of hydride Rb2AsSnH6 perovskites: DFT insights," International Journal of Hydrogen Energy, vol. 133, pp. 225-234, 2025/06/02/, 2025. https://doi.org/10.1016/j.ijhydene.2025.04.308

[87] L. Wei, X. Dong, M. Ma, Y. Lu, D. Wang, S. Zhang, D. Zhao, and Q. Wang, "Co3O4 hollow fiber: An efficient catalyst precursor for hydrolysis of sodium borohydride to generate hydrogen," International Journal of Hydrogen Energy, vol. 43, no. 3, pp. 1529-1533, 2018/01/18/, 2018. https://doi.org/10.1016/j.ijhydene.2017.11.113

[88] Z. Niu, V. J. Pinfield, B. Wu, H. Wang, K. Jiao, D. Y. Leung, and J. Xuan, "Towards the digitalisation of porous energy materials: evolution of digital approaches for microstructural design," Energy & environmental science, vol. 14, no. 5, pp. 2549-2576, 2021. https://doi.org/10.1039/D1EE00398D

[89] N. Xu, Y. Chen, S. Chen, W. Zhang, S. Li, R. Song, and J. Zhang, "First-principles investigations for the hydrogen storage properties of XVH3 (X=Na, K, Rb, Cs) perovskite type hydrides," Journal of Materials Research and Technology, vol. 26, pp. 4825-4834, 2023/09/01/, 2023. https://doi.org/10.1016/j.jmrt.2023.08.218

[90] J. Yuan, Z. Lv, Q. Lu, Y. Cheng, X. Chen, and L. Cai, "First-principles study of the phonon vibrational spectra and thermal properties of hexagonal MoS2," Solid State Sciences, vol. 40, pp. 1-6, 2015/02/01/, 2015. https://doi.org/10.1016/j.solidstatesciences.2014.12.004